# Impact of non-perfect nulls on the detectable population by the LIFE space mission

Xavier Kervyn[1]

Supervisors: Dr. Sascha P. Quanz[*], Felix Dannert[*]

**Abstract**

_Context_. The Large Interferometer For Exoplanets (LIFE) space mission aims at detecting and characterizing the atmospheres of hundreds of nearby extrasolar planets by means of a mid-infrared nulling interferometer concept. To quantify the scientific potential and define the technical requirements inherent to LIFE, the team has developed a software tool to simulate LIFE observations: LIFEsim. This paper aims at integrating imperfect nulls into the simulation software, thereby allowing to measure and quantify the effects on the yield detection of LIFE of an incomplete nulling of the different photon noises in the interference fringe pattern.

_Methods_. The function involved in the combination of the different beams in the interferometer has been modified via the parameter $\delta$ to account for the incomplete nulling, that is to say non-zero nulls in the destructive regions of the transmission map. Simulations have been run for different instrument and yield optimization scenarios. Different stellar and planetary properties of the yield population were eventually considered in order to characterize the impact of non-perfect nulls on the detectable planet population.

_Results_. The detection yield is not significantly affected for $\delta \leq 10^{-6}$. Certain types of host stars were found to provide habitable planets only within restricted regions in parameter space, thereby showing different sensitivities to imperfect nulling. Cold planets showed a better resistance to photon leakage, while low contrast, high angular separation and distant systems were more affected by the latter. Non-zero nulls thus induce a decrease in the "scope" achieved by the instrument. Temperature and angular separation overall seemed to have a weaker impact on the detection yield. The instrument and time distribution scenarios presented discrepancies in the response to $\delta$, with the second scenario and the pessimistic settings not allowing for the detection of habitable planets around F-type stars.

**Keywords**

LIFE Space Mission — LIFEsim — instrumentation noises — observation yield — imperfect nulling

[1]xkervyn@student.ethz.ch
[*]_Institute for Particle Physics and Astrophysics, Exoplanets and Habitability Group, ETH Zürich, Switzerland._

## Contents

## Introduction

The Large Interferometer For Exoplanets (LIFE) space mission was initiated in 2017, with the aim to allow humankind to detect and characterize the atmospheres of hundreds of nearby extrasolar planets, including dozens that are similar to Earth. The project relies on direct imaging techniques to assess the habitability of extrasolar planets and search for bio-markers. However, at the mid-infrared wavelengths used for detecting planets orbiting distant stars, a star is millions of times brighter than an Earth-sized planet. Hence, in order to directly detect the light from the planet, it is necessary to remove most of the light coming from the star. Nulling interferometry is a technique that allows to suppress the light it without appreciably suppressing the light from the planet. Its principle is to produce a destructive interference along the line of sight so that the stellar flux is rejected and the star "nulled out", while the flux of the off-axis source can be transmitted.

To do so, it is crucial to retrieve thermal emission spectra with sufficient spectral resolution, wavelength coverage and sensitivity. LIFE's interferometer concept consists of four formation flying collector telescopes with a beam combiner spacecraft at their center[1] (dual Bracewell nulling interferometer configuration). LIFE mission's scientific potential can be assessed using LIFEsim, a software tool developed to simulate LIFE observations [1]. The latter allows for a simulation of the instrument and the astrophysical sources but does not yet simulate the instrument-related noises. The photon fluxes and signal-to-noise ratio (SNR) of the selected planetary population are eventually computed.

In practice, various instrumental perturbations can degrade the nulling performance. To compensate for the imprecision of the instruments, a SNR greater or equal than 7 is required for a planet to be considered detected, instead of the common lower bound value of 5. This paper investigates the effects of non-zero nulls on the detection yield of LIFE and is thereby a first step taken towards integrating instrumental noise effects in LIFEsim.

## 1. Methods

The model implemented in the software for the transmission maps of the instrument has been described by Ottiger *et al.* [2]. It is the result of the interference of the instrument beams. Adding a phase shift into one arm or several arms of the interferometer array allows to achieve destructive interference for a source on the axis of the instrument. Instead of the usual bright fringe, this results in a dark fringe at the origin of the two dimensional transmission map. The star to be nulled out is centred on the deep central null. The interferometer can be rotated around the observed star-interferometer axis or the signal can be chopped to modulate the intensity signal of a companion by a known periodic function. The transmission function was first modified to account for the aforementioned imperfect nulling.

### 1.1 Modification of the transmission map

A focus has been given on the intensities of the third and fourth destructive output transmissions modes, respectively $T_3$ and $T_4$, given by

$$T_m = |W_m|^2 = \left| \sum_k U_{m,k} V_k \right|^2,$$

with $m = 3, 4$ the chosen output mode, $V_k$ the input beams to be combined by the interferometer and $U_{m,k}$ the matrix element ($m^{\text{th}}$ row, $k^{\text{th}}$ column) implementing the combination of the beams by the central combiner spacecraft [2]. These outputs showcase the odd symmetry of planetary sources in contrast to the pure evenly-symmetric sources such as exo- and local-zodiacal dust and the host star. As a matter of fact, asymmetry of a transmission map allows to separate the planetary signal

from the signal of a symmetric dust/stellar disk around the star by rotation or modification of the transmission map [3]. The differential transmission map $T_{\text{dif}}$, will not be manipulated in this study but will be affected through the relation $T_{\text{dif}} = T_3 - T_4$.

Following the calculations detailed in Ottiger *et al.* [2], the unmodified transmissions maps are respectively given by

$$T_3(\alpha, \beta) = \sin^2 \left( \frac{2\pi L \alpha}{\lambda} \right) \cos^2 \left( \frac{2qL\beta\pi}{\lambda} - \frac{\pi}{4} \right) \quad (1)$$

and

$$T_4(\alpha, \beta) = \sin^2 \left( \frac{2\pi L \alpha}{\lambda} \right) \cos^2 \left( \frac{2qL\beta\pi}{\lambda} + \frac{\pi}{4} \right), \quad (2)$$

with $(\alpha, \beta)$ the angular coordinates describing the position on the sky, $\lambda$ [m] the central value of the spectral bins in the wavelength regime, $L$ [m] representing half of the array's nulling baseline $b$ [m] and $q$ the ratio between the imaging baseline and the nulling baseline of the interferometer. The beam combination of the interferometer can be seen in Fig. 1. Imperfect nulling in the destructive regions shall be modelled in the following.
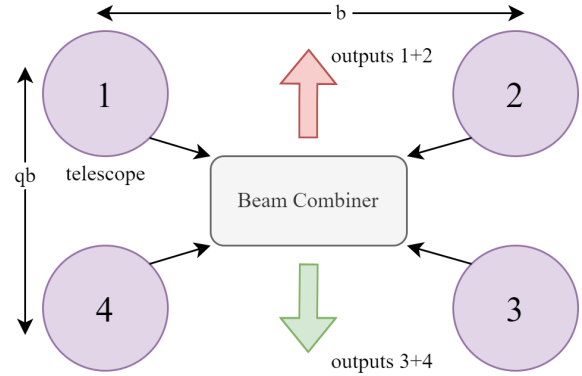


**Figure 1.** Beam combination scheme of the LIFE array.

**Homogeneous modification** In this study, it is assumed that imperfect nulling affects the transmission maps homogeneously, i.e. that the height of the nulls is the same in all the destructive regions at every point. In particular, this implies that the effect does not vary with the distance to the origin $(0,0)$ of the interference pattern where the host star is placed. Such behaviour can be described by a parameter $\delta$ spanning a range of values to reproduce different degrees of perturbation of the ideal model of described by (1) and (2). The modified transmission maps $\tilde{T}_{3,4}^{\delta}$ then write

$$\tilde{T}_3^{\delta}(\alpha, \beta) = \left\{ \sin^2 \left( \frac{2\pi L \alpha}{\lambda} \right) [1 - \delta] + \delta \right\}$$
$$\times \left\{ \cos^2 \left( \frac{2qL\beta\pi}{\lambda} - \frac{\pi}{4} \right) [1 - \delta] + \delta \right\} \quad (3)$$

---

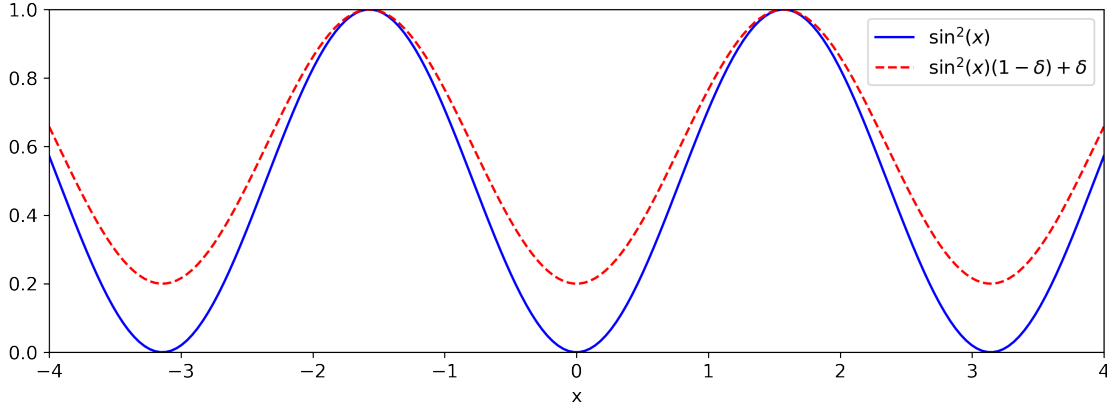[1]https://www.life-space-mission.com/

**Figure 2.** Illustrative plot of the behaviour of the modified transmission function (red dashed line) to the unmodified one (plain blue line), for a simplified transmission function of the form $T(x) = \sin^2(x)$ in one dimension and with $\delta = 0.2$.

and

$$\tilde{T}_4^\delta(\alpha, \beta) = \left\{ \sin^2\left(\frac{2\pi L\alpha}{\lambda}\right)[1-\delta]+\delta \right\}$$
$$\times \left\{ \cos^2\left(\frac{2qL\beta\pi}{\lambda}+\frac{\pi}{4}\right)[1-\delta]+\delta \right\}. \quad (4)$$

An illustrative plot of the modified function can be seen in Figure 2, for a simplified transmission map of the form $T(x) = \sin^2(x)$ in one dimension and with $\delta = 0.2$. This is for illustration purposes as the values considered for the null height $\delta$ throughout this study range from 0 to 0.1. The reason for this cutoff is that significant impact on the detection yield happen for $\delta \leq 0.1$, whereas most of the planets vanish from the instrument outcome for $\delta > 0.1$.

## 1.2 Simulations & Analysis

Once the transmission map modified to $\tilde{T}_{3,4}^\delta$, the simulation was conducted for different values of $\delta$, spanning the model of an ideal interferometer (perfect nulls, $\delta = 0$) to more pessimistic scenarios ($\delta = 0.1$).

The simulation plan follows the different configurations defined in Quanz *et al.* [4]. Two time distribution scenarios were considered, either considering the full parameter space of simulated planets (scenario 1, S1) or restricting the latter to the rocky exoplanets within the Habitable Zone (HZ; scenario 2, S2) of their host star. The ratio between the long and the short baseline of the X-array is of $q = 6 : 1$ and a $\pi/2$ phase shift is applied between the two conjugate transmission maps 3 and 4. Only planets around FGK and M-stars will be considered (by reference to the Morgan-Keenan classification system). The wavelength setting the angular separation of the instrument is of 15 $\mu$m. Different instrument settings were also considered in the study, based on the three scenarios already implemented in the software (baseline, optimistic and pessimistic), which are summarized in Table 1.

Once the time optimization and instrument setting scenarios chosen, the only component varying is the transmission

| Name | Diameter [m] | Wavelength range [$\mu$m] |
|---|---|---|
| Baseline | 2 | $4 - 18.5$ |
| Optimistic | 3.5 | $3 - 20$ |
| Pessimistic | 1 | $6 - 17$ |

**Table 1.** Summary of the different instrument setting scenarios considered, affecting the diameter of the four collecting spacecrafts and the observation wavelength.

map function (via $\delta$). The analysis of the results focuses on the parameters that are essential either to the detection of extrasolar planets or to the assessment of their potential habitability. Namely, the total number of detectable planets was computed with respect to:

– the stellar type of their host star, for planets being in the HZ of their host star;

– the equilibrium temperature of the planet (assuming black-body emission);

– the distance from the system (planet + host star) to the instrument;

– the angular separation star - companion;

for each simulation, time optimization scenario and instrument configuration. Restricting the stellar-type analysis to the number of detectable planets in the Habitable Zone (HZ) instead of considering the whole space of detectable planets, irrespective of them being in the HZ or not, is motivated by the fact that selecting planets only within the HZ should be equivalent to re-scaling the space of parameters of the simulation. The validity of this assumption will be discussed later on in this study. It will furthermore be shown that the number of habitable planets is the limiting factor to be taken into account when investigating the effects of non-perfect nulls on the detection yield of LIFE.

To speed up the calculations, all planets orbiting around A-type stars are removed from the simulation, as well as all planets orbiting around M-type stars at a distance greater than 10 pc. We shall finally introduce the quantity

$$R(\delta) = \frac{N(\delta) - N(\delta = 0)}{N(\delta = 0)} \times 100, \quad [\%] \quad (5)$$

to be interpreted as the relative change in the number $N(\delta)$ of detectable planets with respect to the value obtained when $\delta = 0$ (ideal interferometer). Negative values of $R(\delta)$ must therefore be understood as the relative losses experienced by the given population of planets. It should furthermore be noted that a value of $R(\delta) = -100\%$ implies $N(\delta) = 0$, meaning that planets with the corresponding parameters are not detected anymore. When computed on the restricted parameter space of habitable planets, the number of detected planets shall be referred to as $N_{\text{HZ}}(\delta)$ in the following.

## 2. Results

### 2.1 Time distribution scenario 1

**Habitability**    Figure 3 shows the quantity $R(\delta)$ plotted for different stellar types and considering either the full parameter space of planets or just the restriction of the latter to the space of habitable planets. The results were obtained with
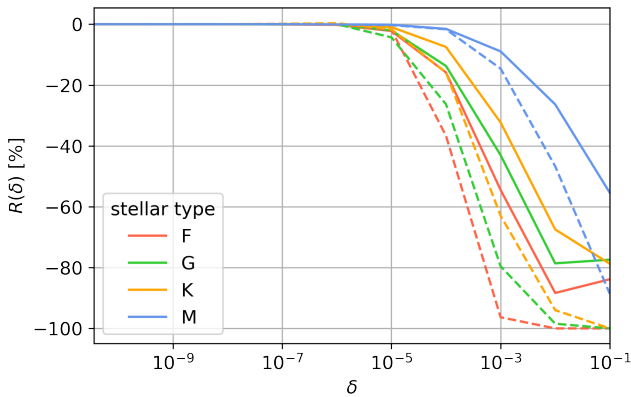


**Figure 3.** Relative change $R(\delta)$ for planets in the HZ (dashed line) or overall (plain line), with the baseline instrument scenario, for different stellar types of the host star.

the instrument set according to the baseline scenario. Similar results were obtained with the optimistic and pessimistic scenarios and can be seen in Appendix, see Section 5.0.2. One can firstly note that the detection yield is not significantly affected for $\delta < 10^{-6}$. The range of $\delta$ plotted will therefore be restricted to the segment $10^{-6} \le \delta \le 10^{-1}$ in the following. For $\delta > 10^{-6}$, one observes a diminution of the number of detectable planets of between 55 to 100% of the initial value for the ideal interferometer ($\delta = 0$).

LIFEsim's yield for habitable planets also decreases more rapidly than the one for planets spanning the whole parameter space. The difference between the two cases reaches about

7% for planets orbiting around M-type star when $\delta = 10^{-3}$ and 33% when $\delta = 0.1$. For planets around K-type stars, one gets respectively 30% and 22% difference at these same two points. The same observation can be made for planets around G and F-type stars. One can also look at the particular value $\delta_\Lambda$ such that

$$R(\delta_\Lambda) = -\Lambda. \quad (6)$$

Choosing $\Lambda = 40\%$, one can see that planets around F-type stars are the first affected by the non-zero nulls of the interferometer ($\delta_{40} \approx 10^{-4}$), followed by planets orbiting around G-type, K-type and M-type stars ($\delta_{40} \approx 10^{-2}$), hence suggesting that imperfect nulling does not affect all planets uniformly but rather depends on the stellar type of their host star. This feature will be further studied in the following.

The detection yield for habitable planets around F, G, K-type stars eventually vanishes after $\delta = 0.1$, while considering the whole space of planets still allows for the detection of about 20 to 40% of the initial population ($\delta = 0$). In light of LIFE's ambitions, this showcases that $N_{\text{HZ}}$ is the limiting factor to be taken into account in this study. The differences that can be noted between the plots for two cases (dashed line versus plain lines in Fig. 3) are most likely to stem from the restrictions on the planet features imposed by considering only habitable planets.

**Stellar type**    Figure 4 shows the number $N_{\text{HZ}}$ of detectable planets in the HZ by LIFEsim, for different values of $\delta$ and different stellar types of the corresponding host star. Results for $0 < \delta < 10^{-4}$ have not been included as the previous analysis of Fig. 3 revealed that such values do not affect importantly the simulation. The vertical axis of the top plot has a linear scale to showcase the yield differences between the stellar types considered, while the bottom one is logarithmic, for this allows for a better estimation of $N_{\text{HZ}}$ when close to zero. M-type stars amount for the larger part of the detection yield, followed by K, G and F-type stars. This can be observed irrespective of the instrument configuration chosen.

As expected, one can see that the optimistic scenario yields the greatest number of detectable planets, followed by the baseline and pessimistic configurations. As already noted in Fig. 3, $N_{\text{HZ}}$ decreases as $\delta \ge 10^{-4}$. At $\delta = 10^{-3}$, the pessimistic configuration does not yield any planet around F-type stars anymore, while the baseline and optimistic settings respectively provide around $10^{-2}$ and $10^{-1}$ such planets. Increasing $\delta$ up to $10^{-2}$ and $10^{-1}$ again leads to further losses in the detection yield with the planets orbiting around F, G and K stars totally or partially vanishing. This phenomenon can be clearly seen on the top plot in Figure 4. At $\delta = 0.1$, the pessimistic configuration only yields one planet in the HZ around a M-type star.

**Temperature**    On Figure 5, the relative change (5) in the number of detectable planets is plotted as a function of $\delta$ and for different groups of equilibrium temperature of the planet. The results shown were obtained with the instrument set to the baseline configuration. The coldest planets ($T < 125$ K)
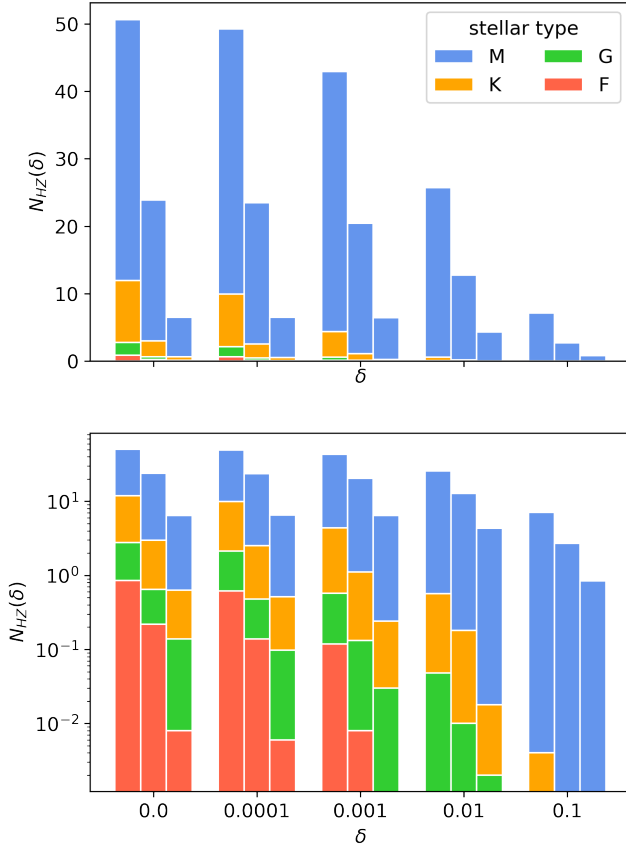
**Figure 4.** Quantity $N_{\mathrm{HZ}}(\delta)$ for different scenarios: optimistic (left), baseline (center) and pessimistic (right).
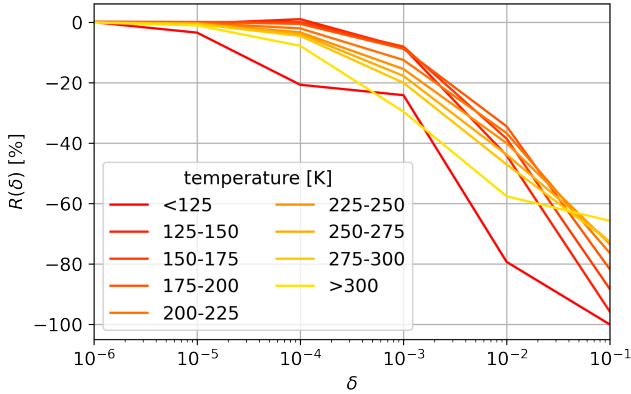


**Figure 5.** Relative change $R(\delta)$ for different ranges of temperature of the planet, in the baseline configuration.

are the first ones to drop, followed by the hottest planets ($T > 300$ K). The other seven groups of planets at a temperature $125 \leq T \leq 300$ K then behave approximately the same under the increase of the perturbation $\delta$.

While the number of detectable planets with $T < 125$ K vanishes as $\delta$ approaches 0.1, it should be noted that planets with $T > 300$ K do not follow the same behaviour and achieve the overall minimal relative change at $\delta = 0.1$. A closer look in the vicinity of $\delta = 0.1$ furthermore reveals that the hotter

the planet, the lesser its population is affected by imperfect nulling in the interferometer.

The same phenomenon can also be observed with the simulations run with the optimistic and pessimistic instrument settings. This is shown in Figures 6 and 7 respectively. The
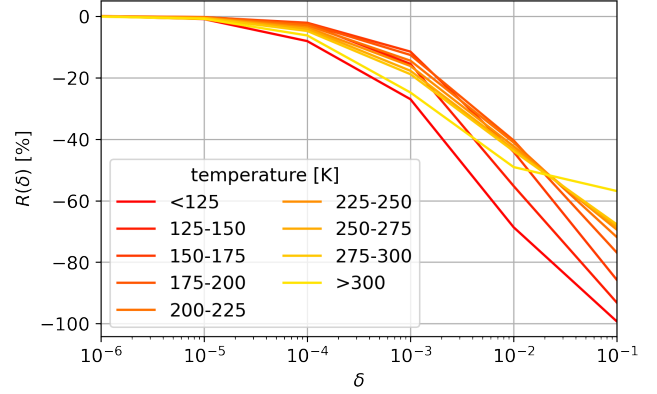


**Figure 6.** Relative change $R(\delta)$ for different ranges of temperature of the planet, in the optimistic configuration.

former seems to favor a similar behaviour of all the groups of temperature under the increase of $\delta$. On the other hand,
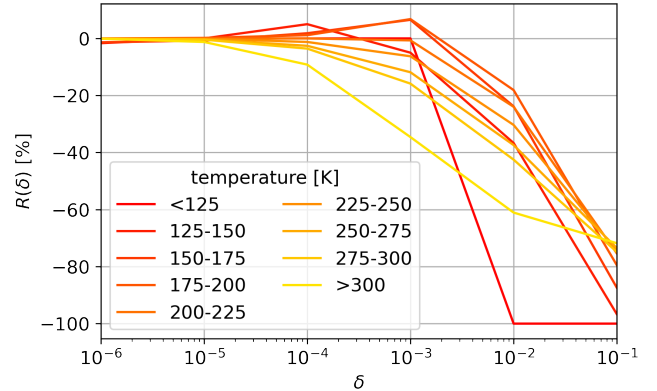


**Figure 7.** Relative change $R(\delta)$ for different ranges of temperature of the planet, in the pessimistic configuration.

pessimistic settings for the instrument clearly induce discrepancies in the response of each group to imperfect nulling. Planets with a temperature $125 \leq T \leq 200$ K experience an increase in their respective number of detected planets for $\delta \leq 10^{-3}$. Summing over all the temperature groups, $N(\delta)$ still decreases, as already seen in Figure 3. This counterintuitive effect is likely to result from a combination of the time distribution scenario with the pessimistic instrument settings, which could allow for the detection of more planets with $T \leq 200$ for a given non-nulling parameter than with the other instrument configurations of Table 1.

**Distance**    The effects of non-zero nulling on different groups of distance from the planet-star system to the instrument were also studied. The results with the instrument set to the baseline

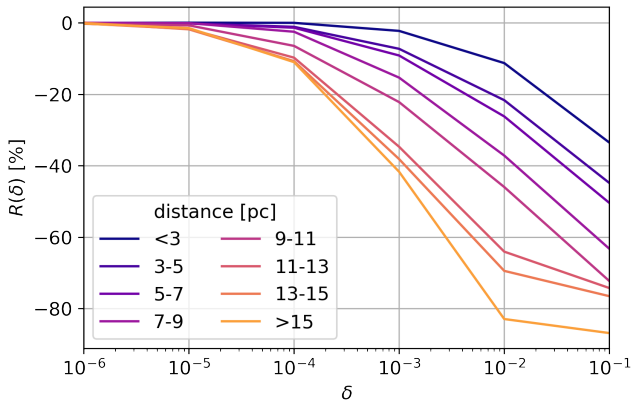configuration are shown in Figure 8. Significant changes to



**Figure 8.** Relative change $R(\delta)$ for different ranges of distance to the instrument, in the baseline configuration.

the detection yield only happen for $\delta \geq 10^{-5}$. The greater the distance $d$ [pc] of the planetary system to the instrument, the more it is affected by non-perfect nulling, i.e. the greater the absolute relative change is for a given null height $\delta$.

Figure 9 shows the results obtained with the instrument set according to the optimistic scenario. It can qualitatively be seen that systems that are closer to the instrument behave approximately the same as in the baseline case, whereas the detection of the farthest systems is improved. On the other hand,
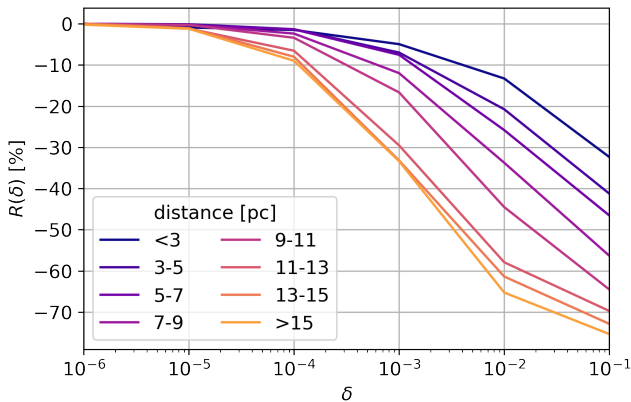


**Figure 9.** Relative change $R(\delta)$ for different ranges of distance to the instrument, in the optimistic configuration.

Figure 10 presents the results obtained when considering the pessimistic scenario for the instrument. Systems located at a distance lesser than 7 pc to the instrument again provide a detection yield similar to the baseline case, while those placed farther away from the instrument are more affected by imperfect nulling. The relative increase in the detection yield that can be noted for $\delta = 10^{-1}$ and $d \geq 11$ pc is again most likely to stem from variations of the detection yield due to the choice of the time distribution scenario.

**Angular separation** The effect of imperfect nulling on the detection yield was finally studied from the viewpoint of
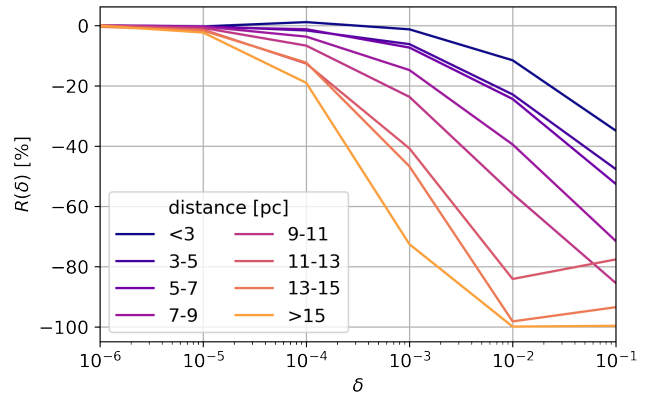


**Figure 10.** Relative change $R(\delta)$ for different ranges of distance to the instrument, in the pessimistic configuration.
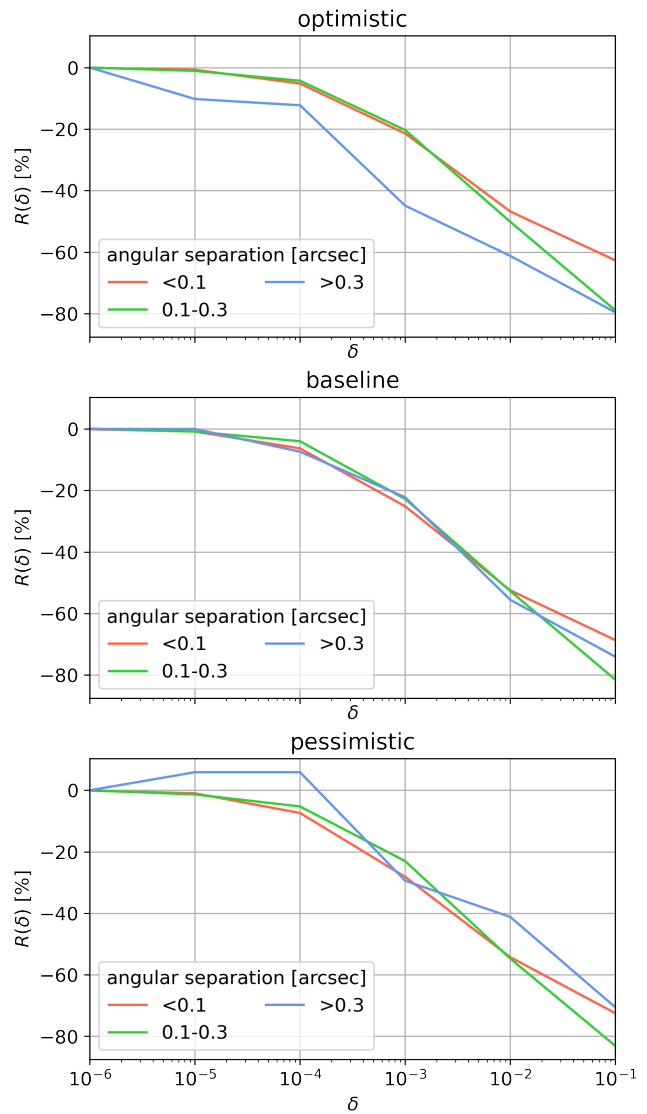


**Figure 11.** Relative change $R(\delta)$, for different subsets of angular separation and for the three instrument scenarios.

the angular separation between the star and its companion. The results of this undertaking are summarized in Figure 11. Differences can be noted as a first glance between the outcome of each instrument scenario.

The planets that are the farthest away from their host star (angular separation greater than 3 arcsec) present discrepancies, the optimistic scenario leading to more important losses for lower values of $\delta$ (in the interval $10^{-6} \leq \delta \leq 10^{-4}$) and the pessimistic showing better results with approximately 20% less relative change and an increase of about 10% of the detectable planet number in the same region. As one approaches $\delta = 10^{-1}$, all scenarios and groups of planets tend towards about 75% relative losses with respect to the initial number of planets detected with a perfect interferometer.

Focusing the attention on each of the different instrument scenarios, one can first see that for the optimistic settings (plain lines), the systems with an angular separation greater than 0.3 arcsec are significantly more affected by imperfect nulling than the other two groups (about 10% additional losses in the detection yield while $\delta \leq 10^{-3}$). In addition, values of $R(\delta)$ obtained for the group with an angular separation comprised between 0.1 and 0.3 arcsec are roughly lying between the ones with $< 0.1$ arcsec (lower bound) and the ones with $> 0.3$ arcsec (upper bound). Systems with an angular separation comprised between 0.1 and 0.3 arcsec overall do not seem to be affected by the change of settings for the instrument. Planets closer to their host star ($< 0.1$ arcsec) show some discrepancies, albeit less distinct, whereas the group orbiting the farthest away ($> 0.3$ arcsec) of their companion show a high sensitivity to the instrument settings.

## 2.2 Time distribution scenario 2

One now looks at the results obtained for the optimization scenario 2, maximizing the number of detectable rocky planets in the Habitable Zone.

**Habitability**    Figure 12 shows the computed number of detectable planets in the HZ by LIFEsim, for different values of $\delta$ and different stellar types of the corresponding host star, analogously to what has already been presented in Fig. 3. The results shown were obtained with the baseline scenario. Similar graphs for the two other scenarios of Table 1 can be seen in Annex, see Section 5.0.2.

The detection yield is not significantly affected by imperfect nulling as long as $\delta \leq 10^{-6}$, after which the number of detectable planets decreases with respect to $N(\delta = 0)$. Moreover, comparing the dashed lines with the plain lines, one notes that restricting the analysis to planets in the HZ of their host star only leads to about 1% additional loss at a given value of $\delta$, irrespective of the stellar type of the host star.

The number of detected planets in orbit around F-type stars vanishes at $\delta = 10^{-3}$, while planets around G-type stars are not detected by the simulation anymore from $\delta = 10^{-2}$, followed by the planets around K-type stars at $\delta = 10^{-1}$. Planets in orbit around M-type stars are again less impacted than the other categories for a given choice of $\delta$, reaching about
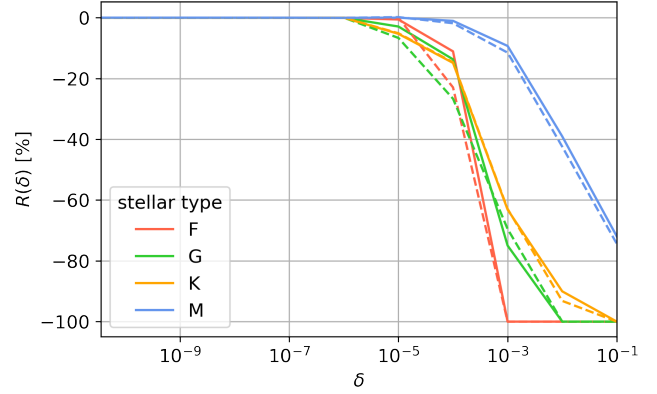


**Figure 12.** Relative change $R(\delta)$ for planets in the HZ (dashed line) or overall (plain line), with the baseline scenario.

70% losses at $\delta = 0.1$. Comparing this with the results of Figure 3, one can already see that S1 favors a better detection of planets around F-type stars at high values of $\delta$ than S2.

It should finally be noted that, for a given stellar type, the the point $\delta_{100}$ for habitable planets coincides with the one for planets spanning the whole planetary parameter space. In other words, the plain and dashed lines cross when $\delta = \delta_{100}$, for each stellar type. The definition of $\delta_{100}$ is here made by reference to (6). As for S1, these results justify the re-scaling of the detection yield to habitable companions.

**Stellar type**    Following the procedure already conducted with S1, one now aims at characterizing the way the choice of the instrument settings scenario affects the detection yield of planets in the HZ of their host star. Figure 13 gathers the results obtained with the three instrument scenarios of Table 1, for different values of $\delta$ and with the four stellar types previously considered. As already observed in Figure 4 for the first optimization scenario, the optimistic instrument settings yield a higher number of detectable planets in the HZ of their host star, followed by the baseline and the pessimistic scenarios. Looking at the bottom figure furthermore reveals that the pessimistic instrument scenario does not yield any planet orbiting in the HZ around a F-type star, even for $\delta = 0$.

The conclusions from the analysis of Figure 12 can also be qualitatively retrieved. As a matter of fact, it is visible on Figure 13 that planets around M-type stars are less affected that the other categories at a given value of $\delta$. While the detectable population in the HZ around M-type stars has decreased of about 10% at $\delta = 10^{-3}$, this values is of about 65% for planets around K-type stars, 75% for planets around G-type stars and already 100% for planets around F-type stars, all when simulating an instrument set to the baseline scenario.

**Temperature**    In Figure 14, the quantity $R(\delta)$ is plotted for different ranges of temperatures of the planet. The results were obtained with the instrument set according to the baseline scenario. As in Figure 5, the population of the coldest planets ($T < 125$ K) is the first one affected by the increase of
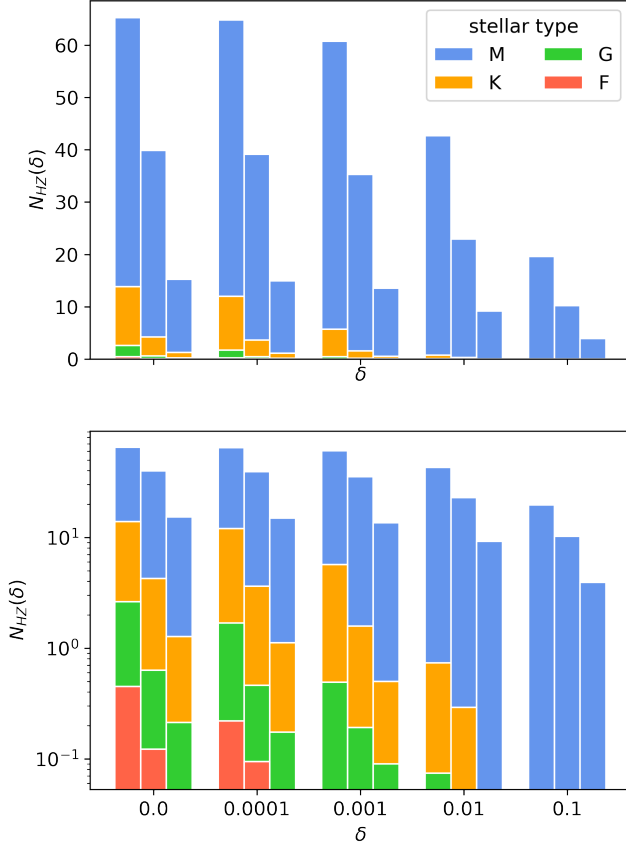
**Figure 13.** Quantity $N_{\mathrm{HZ}}(\delta)$ for different scenarios: optimistic (left), baseline (center) and pessimistic (right).



**Figure 14.** Relative change $R(\delta)$ for different ranges of temperature, in the baseline configuration.
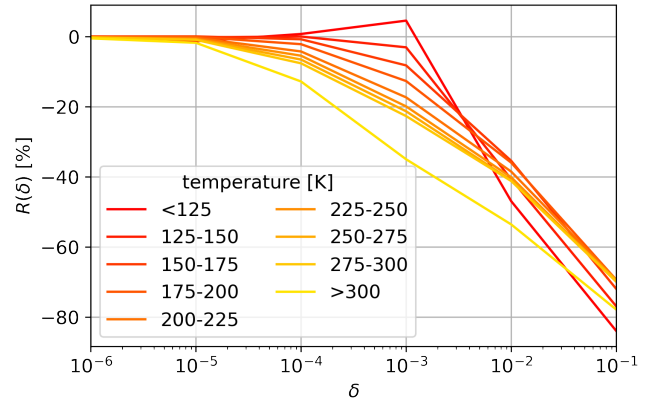


**Figure 15.** Relative change $R(\delta)$ for different ranges of temperature, in the optimistic configuration.
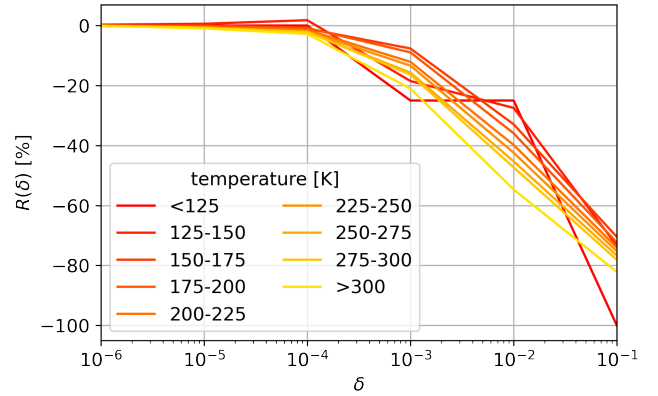


**Figure 16.** Relative change $R(\delta)$ for different ranges of temperature, in the pessimistic configuration.

$\delta$, followed by the the hottest planets ($T > 300$ K). The former decreases by more than 10% when $\delta = 10^{-4}$, while for the latter $R(\delta = 10^{-4}) \approx -4\%$. The other seven groups of planets with a temperature $125 \leq T \leq 300$ K behave approximately the same and experience a relative diminution of their population of between 1% and 2% when $\delta = 10^{-4}$. Increasing $\delta$ up to $10^{-3}$, the number of detected planets with temperature lesser than 125 K increases and the corresponding relative change $R(\delta)$ reaches about $-10\%$. This behaviour could again be induced by the time distribution scenario. The planet population with $T > 300$ K keeps decreasing, with about 22% losses to the initial population ($\delta = 0$) at $\delta = 10^{-3}$. The other seven groups of temperature "broaden", with values of $R(\delta)$ comprised between $-8\%$ and $-18\%$. It can in addition be noted that within this group, planets with an higher temperature are more affected by imperfect nulling of the interferometer. This phenomenon was already observed in Figure 5. As $\delta$ tends towards 0.1, the number of detectable planets keeps shrinking. At $\delta = 10^{-1}$, planets with a temperature comprised within 125 K and 300 K have a similar behaviour and achieve a relative change in their population number of about $R(\delta = 10^{-1}) \approx -75\%$. On the other hand, the two groups of extreme temperatures ($T < 125$ K or $T > 300$ K) experience a greater decrease in their population, respectively yielding a diminution of about $-83\%$ and $-80\%$ of their initial number.

Figures 15 and 16 present the results obtained when conducting the same analysis, respectively with the instrument set to the optimistic or pessimistic configuration. The major discrepancies with respect to the baseline scenario stem from the group of coldest planets ($T < 125$ K) which show a increase in the detection yield for $\delta \leq 10^{-3}$ in Figure 15, and then a

brutal decrease. In Figure 16, it can be seen that this time the second group of planets with temperature $125 \leq T \leq 150$ K is also affected, such that planets with $T \leq 150$ K first experience losses in their detection yield while $10^{-6} \leq \delta \leq 10^{-3}$. It then stabilize around $R(\delta) = -25\%$ while $10^{-3} \leq \delta \leq 10^{-2}$, before shrinking as $\delta$ reaches its upper bound. These differences to the baseline scenario shall be further discussed later on in this report and compared to the results with S1.

**Distance**   Reproducing the work summarized in Figure 8 for S1, the impact of imperfect nulling on various groups of distance from the planet-star system to the instrument was also studied. The instrument was set to the baseline configuration and the results of this undertaking are presented in Figure 17. Note that, based on Figure 12, the range of $\delta$ plotted has again



**Figure 18.** Relative change $R(\delta)$ for different ranges of distance to the instrument, in the optimistic configuration.



**Figure 17.** Relative change $R(\delta)$ for different ranges of distance to the instrument, in the baseline configuration.



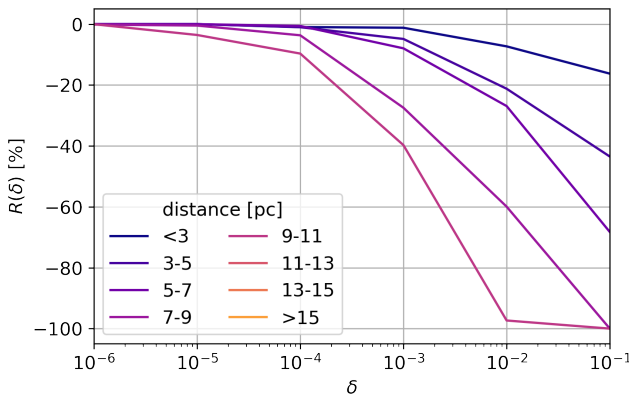**Figure 19.** Relative change $R(\delta)$ for different ranges of distance to the instrument, in the pessimistic configuration.

been restricted to the interval $10^{-6} \leq \delta \leq 10^{-1}$.

Unlike in Figure 8, changes in the detection yield can already be seen for $\delta \leq 10^{-5}$. Moreover, one also notices that only systems at a distance lesser than 11 pc can be detected by LIFE, resulting in an undefined (and hence not plotted) relative change $R(\delta)$ for systems a a distance greater than 11 pc. Nevertheless, it can still be seen that the greater the distance of the planetary system to the instrument, the more it is affected by the non-perfect nulling, i.e. the greater the absolute relative change is for a given value of $\delta$. This phenomenon could already be assessed in Figure 8.

Figures 18 and 19 show the analogous analysis, this time with the instrument set according to the optimistic and pessimistic scenarios respectively. The same conclusions as for the baseline scenario can be drawn, i.e. the systems that are the farthest away from the instrument are the first affected by imperfect nulling and experience a greater relative loss at a fixed height $\delta$. The most notable difference of the optimistic and pessimistic cases with the baseline case lies in the "scope" achieved by the instrument. As a matter of fact, one can see that the optimistic scenario allows for the detection of systems at a distance greater greater than 15 pc, whereas for the pessimistic case all systems at a distance greater than 9 pc are not detected by LIFE. This limitation was not observed in Figures
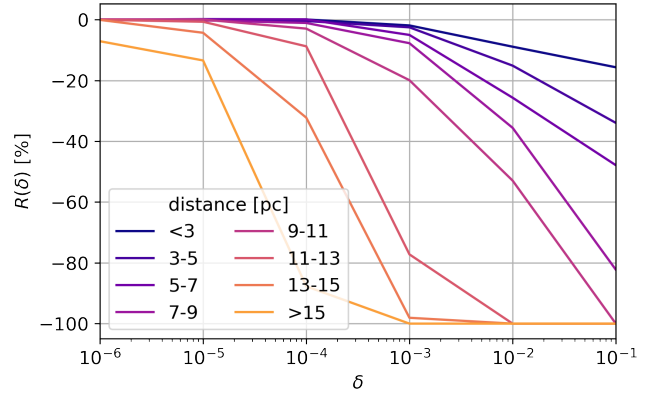
8, 9 and 10 for the first optimization scenario.

**Angular separation**   Figure 20 finally showcases the effects of imperfect nulls on the detection yield of LIFE, from the viewpoint of the angular separation of the planet to its host star. The three scenarios of Table 1 were used.

For planets close to their host star (angular separation lesser than 0.1 arcsec), both the baseline and pessimistic scenarios yield yield very similar results, with less than 1% absolute difference in the relative change of these two configurations throughout the simulation. For $\delta \leq 10^{-2}$, the optimistic instrument settings yield to a greater decrease in the number of detected planets, with about 7% additional relative losses in comparison to the two previous configurations. When $\delta \geq 10^{-2}$, the optimistic case roughly matches the baseline and pessimistic ones, with less than 3% difference between them. The three scenarios eventually converge towards $R(0.1) \approx -78\%$ at the end of the simulation.

The outcome is different for planets with an angular separation comprised between 0.1 and 0.3 arcsec. While the baseline and pessimistic scenarios again match up until $\delta \leq 10^{-3}$ (up to a difference of about 2% in their respective relative change) but then diverge for $\delta > 10^{-3}$, with the baseline sce-

**Figure 20.** Relative change $R(\delta)$ for different groups of planets according to their angular separation to their host star and with the three instrument scenarios.
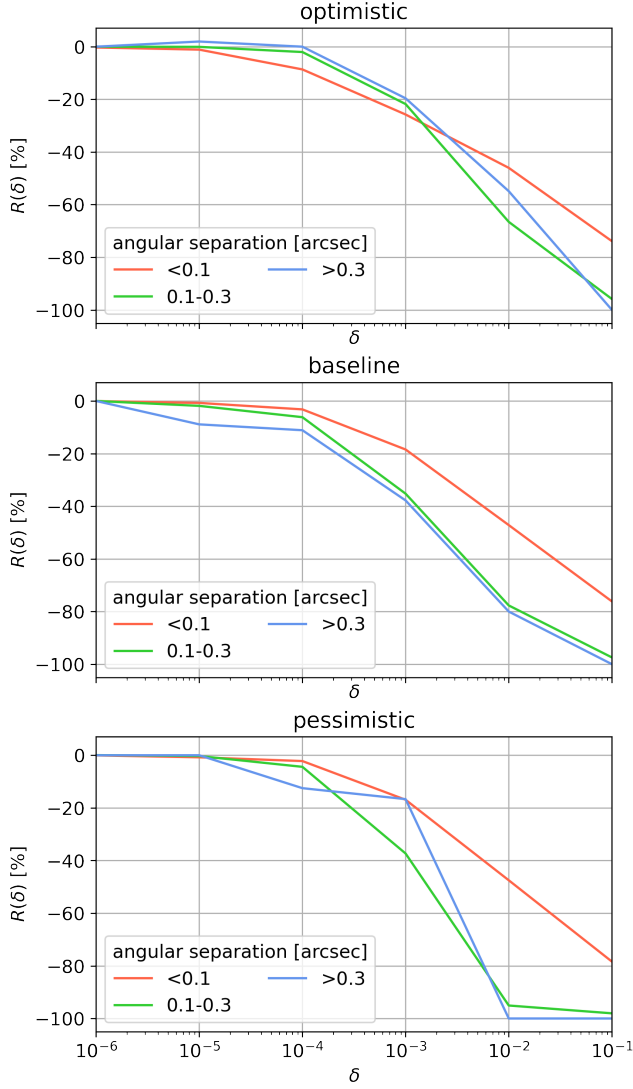
nario providing better results than the pessimistic one. At $\delta = 10^{-2}$, the former yields $R(10^{-2}) \approx -78\%$ and the latter $R(10^{-2}) \approx -95\%$. This discrepancy between the two scenarios vanishes as $\delta$ tends towards its maximal value, and the three instrument scenarios converge towards $R(0.1) \approx -98\%$.

Finally, planets orbiting the farthest away from their host star (angular separation greater than 0.3 arcsec) show again a different behaviour. As long as $\delta < 3 \times 10^{-3}$, the pessimistic scenario yields a relative change bounded between the baseline and the optimistic scenario. The latter two respectively have between 10 and 20% difference, the optimistic one providing better results. As $\delta$ tends towards $10^{-2}$, number of detected planets with the pessimistic scenario vanishes and $R(\delta)$ reaches $-100\%$. With the optimistic and baseline settings however, the relative change to the initial case ($\delta = 0$) reaches about $-55\%$ and $-80\%$ respectively. The three sce-

narios then converge towards $R(\delta) = -100\%$ as $\delta$ approaches its upper bound.

Comparing the behaviours observed for the different subsets of angular separation, one can see that, with an instrument set to the baseline scenario and at a given value of $\delta$, the lower the angular separation, the better the detection yield. For $\delta \leq 10^{-4}$, the outcome of the first two subsets of planets (red and green lines) are very similar, but as $\delta$ reaches $10^{-3}$, the planets with an angular separation comprised between 0.1 and 0.3 arcsec start behaving the same way as planets the farthest away from their host star (angular separation greater than 0.3 arcsec). One does not observe this behaviour with the optimistic and pessimistic instrument settings. The optimistic configuration eventually yields the least-affected detection yield at the upper bound of $\delta$ ($R(0.1) \approx -78\%$), followed by the baseline ($R(0.1) \approx -98\%$) and pessimistic ones ($R(0.1) = -100\%$).

This concludes the presentation of the results obtained in this study. We now aim at interpreting the results obtained with the two different time optimization scenarios and the three instrument configuration modes.

## 3. Discussion

**Restriction to habitable planets** Figures 3 and 12 have shown that restricting the analysis to the space of parameters of habitable planets induced slight changes in the detection yield. It has then been assumed in Figures 4 and 13 that the latter were not significant enough to prevent from focusing the analysis of the stellar-type dependence only on habitable planets. To prove this assumption, let us consider the function

$$Q_N(\delta) = \frac{N_{\mathrm{HZ}}(\delta)}{N(\delta)}. \tag{7}$$

This dimensionless quantity represent the ratio of the number of detected habitable planets by LIFE to the total number of detectable planets. Hence, an horizontal line on the graph of $Q_N(\delta)$ indicates that $N_{\mathrm{HZ}}(\delta) \propto N(\delta)$, thereby assessing the re-scaling hypothesis.

In Figure 21, $Q_N$ is plotted for the two optimization scenarios and four aforementioned stellar types considered in this study. The results were obtained with the instrument set to the baseline configuration. Note that the plots corresponding to S2 do not span the entire range $10^{-6} \leq \delta \leq 10^{-1}$, for the ratio (7) is not defined when $N(\delta) = 0$. In light of the results obtained in Figures 3 and 12, we shall therefore restrict our comment to the interval $10^{-6} \leq \delta < 10^{-3}$. Along this segment, $Q_N$ is approximately constant, except in the case of planets in orbit around G and F-type stars where it varies of about 25% with S2. Hence, it seems reasonable to assume that $N_{\mathrm{HZ}}(\delta) \propto N(\delta)$ in the range of interest for this study.

**Significant values of $\delta$** All the options considered for the time optimization scenarios and instrument settings, with outcomes summarized on Figures 3 and 12 (for the baseline
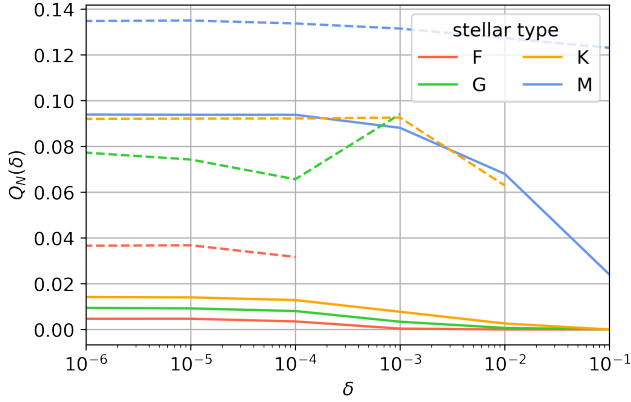
**Figure 21.** Ratio $Q_N(\delta)$ for different stellar types, S1 (plain) or S2 (dashed line) and the baseline configuration.

instrument scenario), showed that significant changes in the detection yield happen for $\delta \geq 10^{-6}$. One now aims at determining the upper limit to be considered for $\delta$.

Although there are supposedly no upper restrictions on the perturbation of the instrument that causes imperfect nulling, one can define the upper limit as the maximal value of $\delta$ such that the simulation still yields planets in the HZ around stars of every type: M, K, G, and F. Figure 21 suggested that after $\delta < 10^{-3}$, it is not efficient to observe even the easiest F-type targets with the baseline instrument configuration. Referring to Figure 3, Figure 12 as well the graphs shown in Appendix, Section 5.0.2, one can record the values of $\delta$ for which a given category of habitable planets is not detected anymore by the simulation, namely $\delta_{100}$. The result of this undertaking is summarized in Table 2. Recall that the results presented

| Optimization | Instrument | F | G | K | M |
|---|---|---|---|---|---|
| | Optimistic | $10^{-2}$ | $10^{-1}$ | $10^{-1}$ | – |
| Scenario 1 | Baseline | $10^{-2}$ | $10^{-1}$ | $10^{-1}$ | – |
| | Pessimistic | $10^{-3}$ | $10^{-1}$ | $10^{-1}$ | – |
| | Optimistic | $10^{-3}$ | $10^{-1}$ | $10^{-1}$ | – |
| Scenario 2 | Baseline | $10^{-3}$ | $10^{-2}$ | $10^{-1}$ | – |
| | Pessimistic | $0.0$ | $10^{-2}$ | $10^{-2}$ | – |

**Table 2.** Order of magnitude of $\delta_{100}$, for planets in the HZ of different stars and the different scenarios considered.

overall showed that the optimistic instrument settings provide better results than the baseline ones, which also provide better results than the pessimistic ones. This was of course to be expected in light of their definition in Table 1 and translates in the fact that, among all optimization scenarios, the pessimistic instrument settings provide the lowest value of $\delta_{100}$. With S1, one retrieves the limit $\delta < 10^{-3}$, while the S2 does not yield any planet in orbit in the HZ around a F-type star even in the case of a perfect interferometer. This phenomenon was already observed in Figure 13 and should be taken into account when defining the scientific objectives of LIFE.

**Planetary properties** When characterizing the effects of imperfect nulling based on different stellar types, one should keep in mind that the latter refer to the Morgan-Keenan classification system, which is based on the color of the star. It is assumed in LIFEsim that stars radiate as black-bodies. Hence, among the categories considered in this study, F stars represent the hottest stars, and M stars the coldest ones. Figures 3 and 12 showed that the planets orbiting around the coldest stars were less affected by imperfect nulling at a given value of $\delta$ than the ones orbiting around hotter stars, irrespective of the optimization and instrument scenarios chosen.

On the other hand, Figures 5, 6, and 7 as well as 14, 15 and 16 revealed that the coldest and hottest planets were the first to decrease under the increase of $\delta$, while other groups of temperature behaved approximately the same. Recall that planets are also treated as black-bodies in the simulation, with their whole surface area radiating with an equilibrium temperature $T$, determined by the luminosity of their host star, their albedo and their orbital separation to their host star [4]. Further investigations on the parameter space of planets thus had to be conducted in order to characterize the effect of imperfect nulling on the detection yield of LIFE.

Figure 22 shows the distribution of detected and habitable planets in parameter space, with S1, for the four stellar types considered, the baseline instrument configuration and $\delta = \{0.0, 10^{-3}\}$. Exoplanets are distributed according to their distance to the instrument and their angular separation to their host star. The color gradient indicates their equilibrium temperature and the size of the marker relates to the radius of the planet. This allows for a better understanding on how each one of these properties relate to each other. The same analysis with S2 can be seen on Figure 23. These plots show that the distribution of habitable planets in parameter space highly depends on the type of their host star as well as the time optimization scenario. One can overall note that the colder the planet, the lower the distance to the instrument needed to keep it detectable. Moreover, low-temperature planets span a wider range of angular separation (up to 0.3 arcsec), which narrows as the distance to the instrument increases. It can also be seen that very few planets with radii lesser than 0.8 Earth radius are found in the simulation outcome.

Focusing the attention on G-type stars, one sees that an increase in $\delta$ leads to the loss of planets located the farthest away from the instrument, thereby showing a decrease in the "scope" achieved by the latter. This is in concordance with the observations made in Figure 5 and 8, where the hottest and farthest planets were affected earlier by imperfect nulls. A larger value of $\delta$ also seems to prevent the detection of the planets that are closer to their host star, but does not significantly affect the ones with an angular separation greater than 0.2 arcsec.

Turning to planets around K-type stars, one can see that the latter cover the biggest surface of parameter space. Coldest planets are again present only at low distances to the instrument but present angular separations up to more than 0.3

**Figure 22.** Parameter space distribution of the detected and habitable planets, with the time distribution scenario 1, for different types of stars $\delta \in \{0.0, 10^{-3}\}$ and the baseline instrument scenario. Temperature is in Kelvin, planet radii in units of Earth radius.

arcsec. Unlike to G-type stars, one can find such planets close to the instrument and with a low angular separation ($< 0.1$ arcsec). Increasing $\delta$ again mostly leads to losses among the population of planets at a distance greater than 12 pc. Angular separation and temperature are again correlated, such that

high-temperature bodies are the ones with the lowest angular separation. Planets close to their host star are again more affected by imperfect nulling. This can be observed across the whole range of distance to the instrument.

As could already be seen in Figure 4, F-type stars account

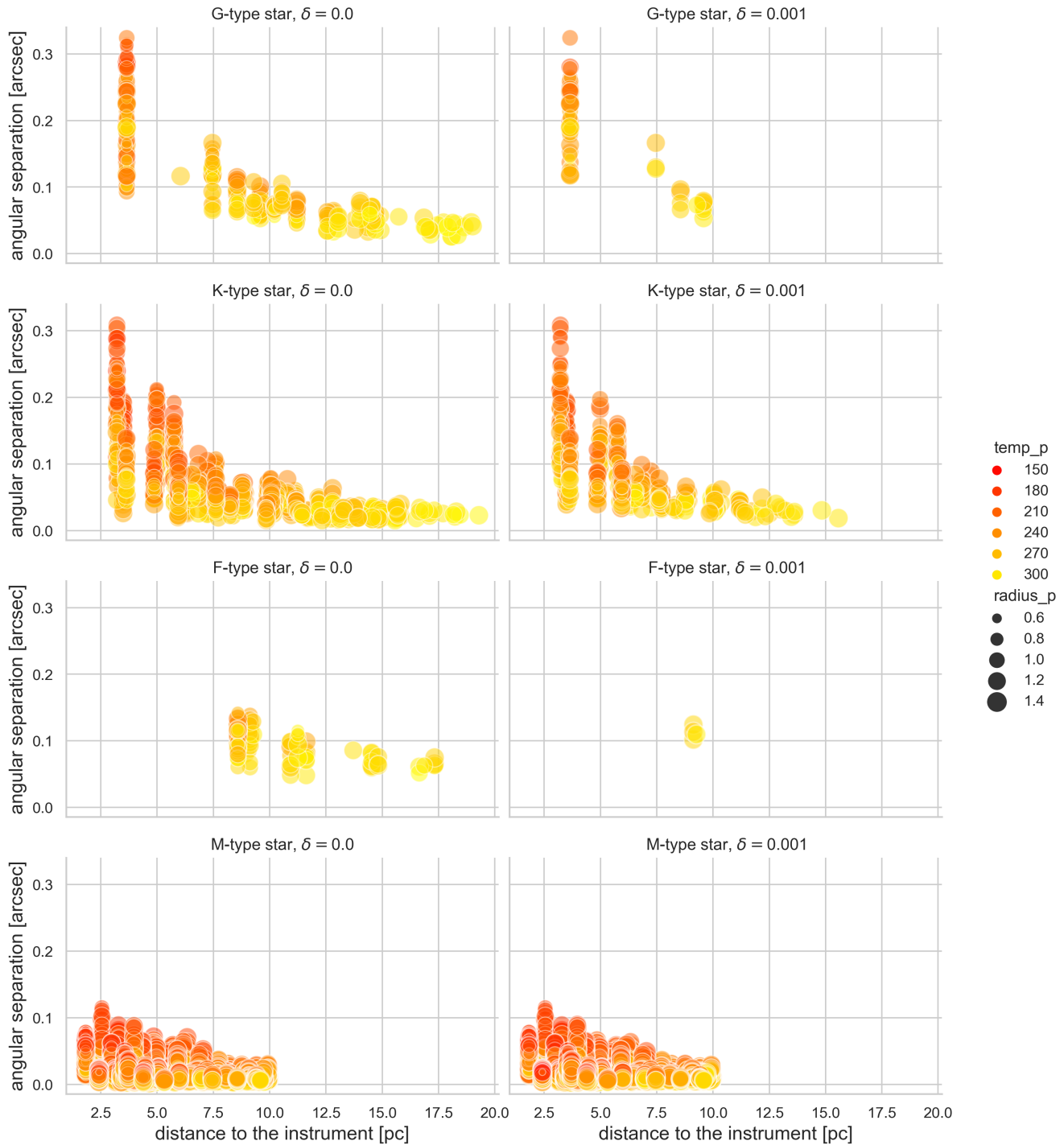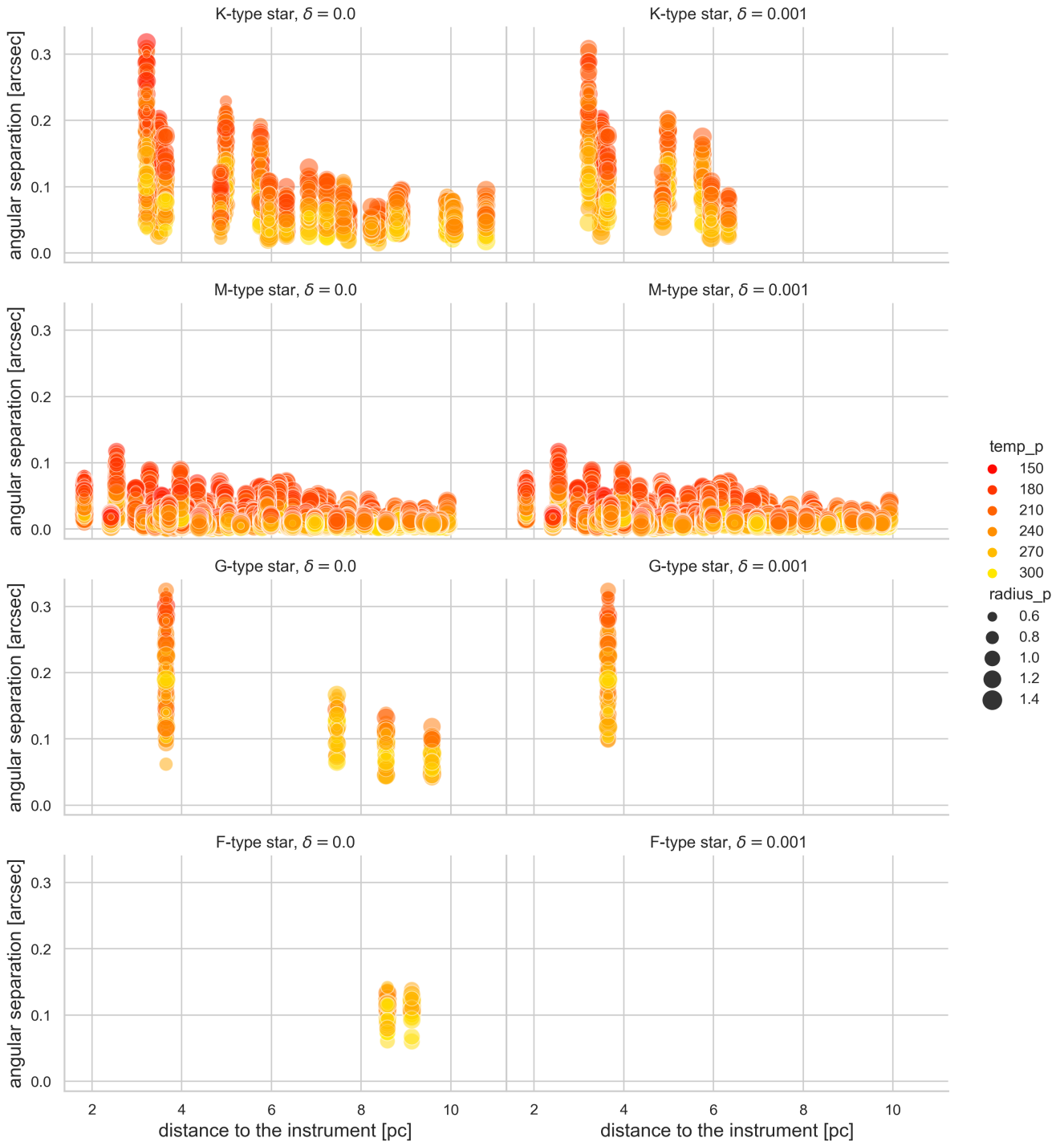**Figure 23.** Parameter space distribution of the detected and habitable planets, with S2, for different types of stars $\delta \in \{0.0, 10^{-3}\}$ and the baseline instrument scenario. Temperature is in Kelvin, planet radii in units of Earth radius.

for the lowest detected population by life. As a matter of fact, Figure 22 shows that planets around the latter stars occupy a narrow range of temperature ($T \geq 270$ K), distance (8 pc $\leq d \leq 17.5$ pc) and angular separation ($0.5 - 1.5$ arcsec) in parameter space. Moreover, the latter parameters correspond to the categories that have shown to be the more affected by

imperfect nulling. The habitable population around F-type stars eventually shrinks to a few planets with temperature $T \geq 300$ K, angular separation of about 1 arcsec and at a distance of around 8 pc to the instrument as $\delta$ reaches $10^{-3}$.

Habitable planets orbiting around M-type stars also occupy a restricted region of parameter space, with a distance

$d \leq 10$ pc to the instrument, lower temperatures than the other groups of stars and hence angular separation up to about 0.1 arcsec only. However, these parameters have shown to be the ones coping the best with imperfect nulling (cf. Figs. 3 and 4) and one can again see that this population has not significantly changed at $\delta = 10^{-3}$ unlike to planets around F-type stars.

Considering now S2 with results shown in Figure 23, one can see at a first glance that the planet distributions differ a lot from the ones observed in Figure 22. G-type stars do not initially ($\delta = 0.0$) provide planets distributed across the whole range of distance to the instrument anymore, but instead at four different distances to the instrument, with each distance comprising planets with a wider range of angular separations than for the first case. In addition, one notes that habitable planets are only found at a distance of up to 12 pc from the instrument, whereas with the first case the farthest habitable planets were located at approximately 18 pc from the instrument. The temperatures are also affected by the change of time distribution scenario, as more colder planets are detected at greater distances to the instrument. Only a few number of planets appear to have an equilibrium temperature greater than 300 K. The habitable planet distribution being different, the effect of imperfect nulling on the detection yield is also different: planets that are the closest to their star still disappear as $\delta$ increases, along with the farthest planets, even though the latter have a lower temperature than with the first scenario. The same observations and conclusions can be drawn when looking at K-type stars.

Planets in orbit around F-type stars again account for the most restricted initial region in parameter space, but this time with distances of about 9 pc and temperatures greater than 270 K. The angular separation is again comprised within 0.5 and 1.5 arcsec. At $\delta = 10^{-3}$, no more habitable planets are observed. This was already shown in Figure 12.

Finally, the distance distribution of M-type stars is radically different, with planets spanning about 1 pc to 10 pc. Recall however that all planets around M-type stars have been excluded from the simulation to speed up calculations. Although this has no influence of the detection yield computed with the first time distribution scenario, this limit actually impacts the simulation outcome of the second time distribution scenario. Habitable planets found around M-type stars again have an angular separation lower or equal than about 0.1 arcsec, equilibrium temperatures mainly below 270 K and show no significant decrease due to imperfect nulling.

**Instrument configuration**   The above planetary properties have been discussed for simulations run with an instrument set to the baseline configuration. We shall now explore the effect of the choice of the instrument on the initial habitable planet distribution. Figure 24 encompasses the distributions obtained for all instrument and time distribution scenarios when $\delta = 0$. Detected and habitable planets are again distributed according to their distance to the instrument and their angular separation to their host star. A color gradient indicates their equilibrium temperature. All stellar types are considered.

The optimistic configuration clearly yields the highest number of habitable planets, irrespective of the time distribution scenario chosen, as already seen on Figures 4 and 13. The planets are the most widely spread across the ranges of temperature, distance and angular separation.

Turning to the baseline configuration, it can be seen that the range of distance of the system to the instrument is greatly impacted. With the first time distribution scenario, only planets with an equilibrium temperature $T \geq 300$ K subsist at a distance greater than 10 pc, whereas in the second case almost all planets previously found in this range of distance with the optimistic settings have vanished. The region of parameter space with $d \leq 10$ pc does not seem to be significantly impacted by the change of time distribution scenario, irrespective of the angular separation.

Considering the pessimistic situation leads to further losses in the detection yield. With the first time distribution scenario, all planets at $d \geq 10$ pc have vanished and the coldest planets ($T \approx 160$ K) are significantly decreased in number. With the other time optimization scenario, the distance threshold is even lower, with no habitable planets detected for $d \geq 8$ pc. The number of cold planets also seems to have diminished.

This matches the results of Figures 8, 9, and 10, which showed that the greatest variation of in the detection yield while changing the instrument settings happened for the planets located the farthest away from the instrument. Restricting the plot to habitable planets in Figure 24 instead of considering all detected planets has furthermore showcased the same "scope" restriction with S1, that could already be noted from Figures 17, 18 and 19 for S2. In addition, one could also observe on Figures 5 to 7 and 14 to 16 that a change in the instrument scenario has a weak impact on the detection yield seen as a function of the temperature of the planet.

**Contrast and resolution**   Under the assumption of blackbody behaviour, LIFEsim computes the luminosity $L_s$ [W] of the stars simulated using Stefan-Boltzmann's law. The resulting flux $F_S$ that passes through the instrument at a distance $d$ [m] is then given by

$$F_s = \frac{L_s}{4\pi d^2}. \tag{8}$$

Taking the ratio $F_p/F_s$ of the planetary flux to the stellar flux, one gets a measure of the contrast of the planet to its host star. Figure 25 shows the contrast-to-angular separation distribution of the detected and habitable planets with the two time distribution scenarios, the instrument in the baseline configuration and different values of $\delta$. Colors indicate the stellar type of the planet's host star. $F_p/F_s$ being of the order of $10^{-6}$, a logarithmic-logarithmic scale has been chosen to better showcase the effect of non-zero nulls.

Starting with an ideal interferometer at $\delta = 0$, one can see that G-type stars account for a majority of habitable planets with an angular separation comprised 0.15 and 0.35 arcsec. A few habitable planets around F-type stars are found in the vicinity of 0.13 arcsec, as well as around K-type stars in the
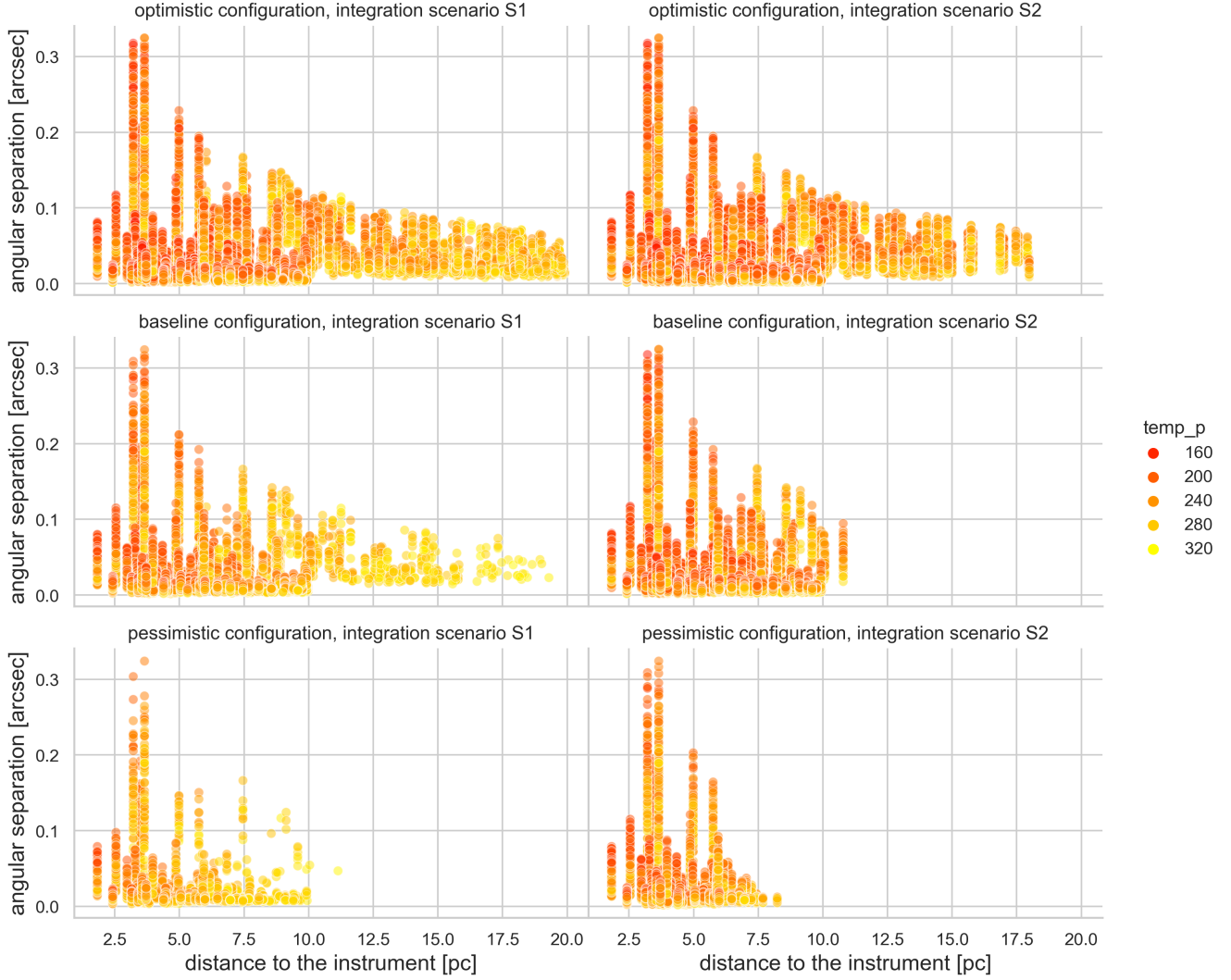
**Figure 24.** Distribution in parameter space of the detected and habitable planets by LIFE, for $\delta = 0$, the two time distribution scenarios and the three instrument configurations mentioned in this study. Planet temperatures are in Kelvin.

range of 0.2 to 0.3 arcsec. However, all these planets have a contrast of less than $10^{-8}$, meaning that their signal is very faint in comparison to the one of their host star. In comparison, M-type stars yield planets with an angular separation comprised between 0.01 to 0.12 arcsec but with higher contrast rates. As a matter of fact, for planets found the closest to such stars, the latter ratio rises up to around $1.8 \times 10^{-6}$, i.e. almost twenty times bigger than for the other stellar types. One overall notes that the smaller the angular separation, the greater the contrast for habitable planets. This can be observed irrespective of the time distribution scenario chosen.

Increasing $\delta$ up to $10^{-3}$, one notices that the populations of habitable planets around F, K and G-type stars have slightly decreased. Although systems with an angular separation greater than 0.2 arcsec seem to be the most affected by the increase of $\delta$ with S1, this must be slightly nuanced in light of the results shown in Figure 11, where one could see that all groups behaved approximately the same in the baseline

scenario. With S2 however, the planets orbiting the farthest away from their host star proved to be more affected by imperfect nulling, as could be seen in Figure 20 for the baseline scenario. One also notes that an increase in $\delta$ leads to a rise of the minimal contrast threshold of the habitable and detected population. At $\delta = 0$, the latter is of the order of $10^{-10}$. It then climbs up to $10^{-9}$ at $\delta = 10^{-2}$ and eventually reaches $10^{-8}$ at $\delta = 0.1$. Due to their initial distribution in contrast-angular separation space, only planets around M-type stars subsist as $\delta$ augments.

As $\delta$ reaches $10^{-2}$ and $10^{-1}$, K-type and G-type stars are successively lost. Planets with low contrast ($F_p/F_s < 10^{-8}$) and medium-high angular separation (greater than 0.08 arcsec) seem to be more affected. This is in concordance with the results obtained in Figure 20, where it could be observed that the planets around M-type stars with the lowest angular separation were the ones coping the best with $\delta$.
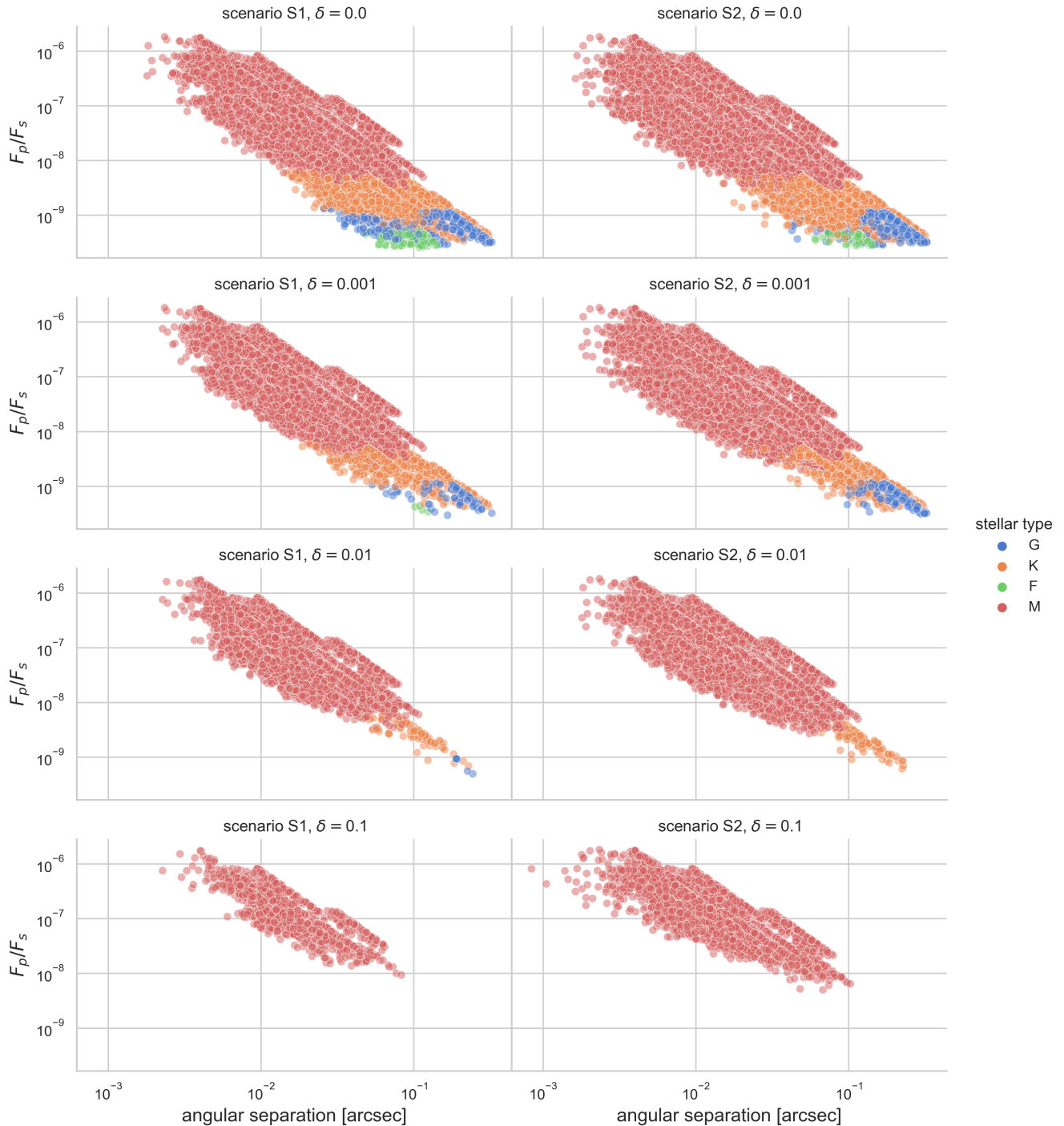
**Figure 25.** Logarithmic - logarithmic contrast-to-angular separation distribution of the detected and habitable planets with the two time distribution scenarios, the instrument in the baseline configuration and different values of $\delta$.

## 4. Summary and conclusions

**Planetary properties** All analysis conducted in this report assessed that the detection yield is not significantly affected for $\delta \leq 10^{-6}$. The different regions of the parameter space of detected planets have then shown different responses to imperfect nulling. This is of great importance as certain types of host stars provide habitable planets only within restricted ranges of temperature, angular separation and distance to the instrument, thereby showing different sensitivities to imperfect nulling. This is in particular the case of F-type stars, whose corresponding planet properties cause the number of detected planets to vanish firstly. On the other hand, the detection yield of planets around M-type stars has proven to be less

impacted under the increase of $\delta$ than all the other categories.

This study has also allowed a further fine-tuning of the measure of the impact of imperfect nulling depending on various stellar and planetary properties. In particular, it has been seen that the hottest or coldest planets were overall the first ones to decrease in number as $\delta$ augmented. However, planets with a temperature around 225K (approximately in the middle of the temperature range) showed a less marked change under the increase of $\delta$. Planets with a low angular separation to their host star showed a higher sensitivity to the perturbed transmission map, gradually disappearing from the detection yield. Besides, detected and habitable systems located far away from the instrument were found to be allowed lower angular separations than those close from the instrument. In other words, nearby habitable planets were found in a wider range of angular separation, that narrows towards low angular separation as the distance to the instrument is increased. Studying the contrast of the planet to its host star however revealed that low-contrast systems were the first lost in the detection yield due to non-zero nulls in the transmission map and that habitable and detectable planets with a low contrast were located at a greater distance from their star. The great role played by the distance of the system has been showcased in many occasions throughout this paper. More specifically, it has been noted that the greater the distance to the instrument, the greater the losses in the detection yield at a given value of $\delta$. All planet properties relate to each other, in such a way that cold but habitable planets were mostly found in systems located at a low distance to the instrument.

**Detection of M-type stars**   The features associated with habitable planets orbiting around M-type stars were found to make the latter more "resistant" to imperfect nulling. M-type stars amount for the larger part of the habitable detection yield in this report, followed by K-, G-, and F-type stars, irrespective of the instrument configuration chosen. And while habitable planets around F-type stars vanish from $10^{-3}$ with the baseline scenario, one can still detect around 20 such planets around M-type stars when $\delta = 0.1$. However, studies have shown that planets around M-type stars are less likely to potentially host life than those around the other types of stars, hence the restriction to $d \leq 10$ pc to speed up calculations [5]. It is thus crucial for LIFE's detection yield to comprise the four aforementioned stellar types. In particular, Quanz *et al.* showed that 30 planets should be observed in order for the fraction $\eta_{hab}$ of "terrestrial exoplanets that reside in the empirical habitable zone around their host star and provide conditions for liquid water to exist" to be of more than 50% [6]. Observing planets around M-type stars only would thus not be sufficient to guarantee the success of the mission.

**Choice of the time distribution scenario**   This study has shown that $\delta$ should be lesser than $10^{-3}$ (cf. Table 2) to meet the previous requirement, with an instrument set to the baseline or optimistic configuration and the second time distribution scenario. However, the pessimistic scenario does not allow for the detection of any habitable planet around F-type stars. One should thus avoid using pessimistic settings when looking for rocky habitable planets. The discrepancies observed between the different instrument settings have shown that S1 overall allows for bigger values of $\delta$ (cf. Table 2), with a minimal value of $\delta_{100} = 10^{-3}$ to be compared with the one $\delta_{100} = 0.0$ obtained with scenario 2. This study has shown that these differences stem from the different occupations of the parameter space obtained when using the two time distribution strategies.

**Choice of the instrument scenario**   The instrument settings have also shown to have a great role on certain parameters of habitable planets in the detection yield. On the one hand, it has been seen that the configuration greatly impacts the "scope" achieved by the instrument, with the optimistic settings allowing for the detection of farther planets than the baseline and pessimistic ones respectively. On the other hand, the temperature and the angular separation showed a weak dependence on the instrument configuration, translating in hardly distinguishable patterns in Figures 11 and 20 or similar plots in Figures 5 to 7 and 14 to 16. Besides, it could also be noted that the optimistic scenario yielded the greatest number of detectable planets, followed by the baseline and pessimistic ones, irrespective of the time distribution scenario considered. Finally, pessimistic settings have overall seemed more subjected to discrepancies in the detection yield, which could be attributed to the robustness of the simulation in those configurations.

**Instrumental requirements**   The choice of a formation-flying space interferometry concept such as LIFE induces strong technical requirements on the instruments: formation flying spacecrafts require a high angular resolution, starlight suppression requires high contrasts and sensitivity requires passive cooling, low thermal noises and ultra-low noise mid-IR detectors. ESA's PROBA-3 mission will consist of three formation flying spacecrafts maintaining a fixed configuration and should exceed the control requirements of LIFE, while NASA's SunRISE mission should also provide further insights into the technology needed to this end.

This paper showed that the null height should not exceed $10^{-6}$ to avoid significant losses in LIFE's detection yield. Focusing on a wavelength of 10 μm, Martin *et al.* demonstrated a null depth of $8 \times 10^{-6}$, which could be lowered to $10^{-8}$ after post-processing, at room temperature and 10% bandwidth [7]. Although a connection between the null height $\delta$ manipulated in this study and the null depth of LIFE's instrument still has to be established (see suggestions for subsequent research), as the latter is expected to be exposed to a lower thermal background (being passively cooled at a temperature around 40K) this should allow for lower null depths.

Passive cooling techniques are currently investigated by the NICE/LIFE project at ETHZ, which aims to demonstrate the measurement technique and the required nulling performance of LIFE at representative wavelengths and flux ranges,

using cryogenic test facilities. Further developments still have to be made on the ultra-low noise mid-IR detectors. LIFE's requirements are still under study but would likely require the instrument to be five times more efficient than JWST's MIRI instrument, to reach space in late 2021. Finally, the Herschel/Planck mission already achieved a passive thermal cooling of 40K.

**Instrumental perturbations**  Defrère *et al.* showcased the effect of spacecraft vibrations in space nulling interferometry in a study comparing the performances of space and ground-based sites for exozodiacal disc detection [8]. Vibrations of the instrument are indeed likely to induce fluctuations in the differential optical paths and pointing errors, which both give rise to stochastic stellar leakage in the destructive output. These vibrations are caused by disturbance forces which can be either internal or external. In the case of LIFE, where the telescopes would not be structurally connected, such vibrations would arise mainly from the thrusters, the optical delay line, the steering mirrors and the reaction wheels. The external disturbance forces are mainly caused by particulate impacts, solar radiation pressure and charging effects but all these effects are not expected to be dominant at the L2 point.

Matter *et al.* [9] estimated the effects of parasitic interference in nulling interferometry, namely with the study of the crosstalk phenomenon. The latter occurs when multiple parasitic reflections happen inside transmitting optics, and because of diffraction effects related to beam propagation along finite size optics. Their results showed that a coherent crosstalk level of about 1% implies a 20% drop of the signal-to-noise ratio at most. Careful attention should thus be paid to reduce the crosstalk level inside an interferometer and ensure an instrumental stability that provides the necessary sensitivity through calibration procedures.

**Achieving better nulling**  The need to ensure that $\delta \leq 10^{-6}$ translates to extremely tight demands upon the design and fabrication of the instrument: all the four telescopes used must be highly symmetric, their mirrors carefully tailored, sources of contamination must be minimized, optical surfaces must be nearly ideal, and alignments must be extremely precise. Satisfaction of all of these requirements entails substantial cost. Peters *et al.* [10] investigated the potential applications of an adaptive-nulling method in the case of a simple Bracewell interferometer. The proposed method should reduce the cost of building and aligning the highly precise optical components and assemblies needed for nulling. A compensator would be inserted into each optical train, upstream of the location where the output beam from the two telescopes are combined. Each one of these devices could then independently control the amplitude and phase of the electric field of the spatial mode that couples into the detector, thereby correcting for the imperfections in the optical train and in the beam combiner and making it possible to obtain a deep null from an imperfect instrument. Although not tested in space, this approach has been successfully demonstrated in the laboratory, both at near IR and mid-IR wavelengths.

**Subsequent research**  Further investigations remain to be conducted to identify and mitigate the sources of imperfect nulling in the instrument as well as relate the null depth of the latter to the parameter $\delta$ used throughout this work. Other models for the transmission map should also be studied, taking into account especially that $\delta$ could vary with the distance to the point where the star to be nulled out is placed as well as the wavelength of observation.

# Acknowledgments

# References

[1] J. Kammerer et al., 'Simulating the exoplanet yield of a space-based mid-infrared interferometer based on Kepler statistics', Astronomy and Astrophysics, vol. 609, p. A4, Jan. 2018, doi: 10.1051/0004-6361/201731254.

[2] M. Ottiger, et al., 'Large Interferometer For Exoplanets (LIFE): II. Signal simulation, signal extraction and fundamental exoplanets parameters from single epoch observations', Sep. 2021.

[3] Lay, O. P. 2004, Appl. Opt., 43, 6100.

[4] S. P. Quanz et al., 'Large Interferometer For Exoplanets (LIFE): I. Improved exoplanet detection yield estimates for a large mid-infrared space-interferometer mission', arXiv:2101.07500 [astro-ph], May 2021.

[5] F. Dannert, 'Observing strategies for the Large Interferometer for Exoplanets', pp. 13, March 2021.

[6] S. P. Quanz et al., 'Atmospheric characterization of terrestrial exoplanets in the mid-infrared: biosignatures, habitability, and diversity', Exp Astron, Sep. 2021, doi: 10.1007/s10686-021-09791-z.

[7] S. Martin et al., "High performance testbed for four-beam infrared interferometric nulling and exoplanet detection," Appl. Opt. 51, 3907-3921 (2012)

[8] D. Defrère et al., 'Nulling interferometry: performance comparison between space and ground-based sites for exozodiacal disc detection', A&A, vol. 490, no. 1, pp. 435–445, Oct. 2008, doi: 10.1051/0004-6361:200810248.

[9] A. Matter, D. Defrère, W. C. Danchi, B. Lopez, and O. Absil, 'Parasitic interference in nulling interferometry', Monthly Notices of the Royal Astronomical Society, vol. 431, no. 2, pp. 1286–1295, May 2013, doi: 10.1093/mnras/stt246.

[10] R. D. Peters, O. P. Lay et al., "Adaptive nulling for the Terrestrial Planet Finder Interferometer", Proc. SPIE 6268, Advances in Stellar Interferometry, 62681C (28 June 2006); https://doi.org/10.1117/12.672170

# 5. Appendix

### 5.0.1 Modified code

To simulate imperfect nulling, the parameter $\delta$ (delta) has first been added among the options in `options.py`.

```
1  # parameter accounting for the non-perfect nulling
2          delta = self.data.options.other['delta']
```

It is initialized to $\delta = 0.0$ and remains unchanged by default.

```
1      def __init__(self):
2          [...]
3
4          self.other = {'image_size': 0,
5                        'wl_optimal': 0.,
6                        'n_plugins': 0,
7                        'delta': 0.}  # the parameter delta accounts for the non-perfect nulling
8          [...]
```

It can then be easily set to a certain value before running a simulation through the command `options.set_manual()`. The script below is an example of the code used to run simulations with $\delta$ spanning 0 to 0.1.

```
1  import lifesim
2  import numpy as np
3
4  # MODIFIED TRANSMISSION MAP
5  # ---------- Set-Up ----------
6
7  # create bus
8  bus = lifesim.Bus()
9
10 # setting the options
11 bus.data.options.set_scenario('pessimistic')
12 # changing to optimization scenario 1
13 bus.data.options.optimization['habitable'] = False
14
15 # set options manually
16 # bus.data.options.set_manual(diameter=4.)
17
18 # ---------- Loading the Catalog ----------
19
20 bus.data.catalog_from_ppop(input_path='C:/pathtofile/baselineSample.fits')
21 bus.data.catalog_remove_distance(stype=0, mode='larger', dist=0.)  # remove all A stars
22 bus.data.catalog_remove_distance(stype=4, mode='larger', dist=10.)  # remove M stars > 10pc
23
24 # ---------- Creating the Instrument ----------
25
26 # create modules and add to bus
27 instrument = lifesim.Instrument(name='inst')
28 bus.add_module(instrument)
29
30 transm = lifesim.TransmissionMap(name='transm')
31 bus.add_module(transm)
32
33 exo = lifesim.PhotonNoiseExozodi(name='exo')
34 bus.add_module(exo)
35 local = lifesim.PhotonNoiseLocalzodi(name='local')
36 bus.add_module(local)
37 star = lifesim.PhotonNoiseStar(name='star')
38 bus.add_module(star)
39
40 # connect all modules
41 bus.connect(('inst', 'transm'))
42 bus.connect(('inst', 'exo'))
43 bus.connect(('inst', 'local'))
44 bus.connect(('inst', 'star'))
45
46 bus.connect(('star', 'transm'))
47
48 # ---------- Creating the Optimizer ----------
```

```
49  # After every planet is given an SNR, we want to distribute the time available in the search phase such
        that we maximize the number of detections.
50
51  # optimizing the result
52  opt = lifesim.Optimizer(name='opt')
53  bus.add_module(opt)
54  ahgs = lifesim.AhgsModule(name='ahgs')
55  bus.add_module(ahgs)
56
57  bus.connect(('transm', 'opt'))
58  bus.connect(('inst', 'opt'))
59  bus.connect(('opt', 'ahgs'))
60
61  # parameter accounting for the non-perfect nulling
62  delta_ = np.insert(np.logspace(-10, -1, num=10, base=10), 0, 0, axis=0)
63  for val in delta_:
64      print(val)
65      # set the value for delta to be used in the simulation
66      bus.data.options.set_manual(delta=val)
67
68      # ---------- Running the Simulation ----------
69
70      # run simulation. This function assigns every planet an SNR for 1 hour of integration time. Since
71      # we are currently only simulating photon noise, the SNR will scale with the integration time as
72      # sqrt(t)
73      instrument.get_snr()
74
75      opt.ahgs()
76
77      # ---------- Saving the Results ----------
78
79      bus.data.export_catalog(output_path=f'C:/pathtofile/filename_delta={val}.hdf5')
```

The parameter $\delta$ should directly act on the expressions for the 3rd and 4th transmission maps in `transmission.py` defined by (3) and (4). The following script shows the implementation of the modified transmission maps.

```
1       # transmission map of mode 3, modified through parameter delta
2       if 'tm3' in map_selection:
3           tm3 = (np.sin(2 * np.pi * L * alpha / wl_bins) ** 2
4                   + delta * (1 - np.sin(2 * np.pi * L * alpha / wl_bins) ** 2)) \
5                   * (np.cos(2 * self.data.options.array['ratio'] * np.pi * L * beta / wl_bins - np.pi /
        4) ** 2
6                       + delta * (1 - np.cos(2 * self.data.options.array['ratio'] * np.pi * L * beta /
        wl_bins - np.pi / 4) ** 2))
7
8       # transmission map of mode 4, modified through parameter delta
9       if 'tm4' in map_selection:
10          tm4 = (np.sin(2 * np.pi * L * alpha / wl_bins) ** 2
11                  + delta * (1 - np.sin(2 * np.pi * L * alpha / wl_bins) ** 2)) \
12                  * (np.cos(2 * self.data.options.array['ratio'] * np.pi * L * beta / wl_bins + np.pi /
        4) ** 2
13                      + delta * (np.cos(2 * self.data.options.array['ratio'] * np.pi * L * beta / wl_bins
         + np.pi / 4) ** 2))
```

One should furthermore ensure that the simulation runs through the modified transmission maps instead of the analytical solution that can be found for an ideal interferometer. This is done in line 8 of the following script.

```
1   def transmission_curve(self,
2                           angsep: float,
3                           phi_n: int = 360):
4       [...]
5       # retrieve the transmission curves
6           (_, _, _,
7            transm_curve_tm4,
8            transm_curve_chop) = self.transmission_map(map_selection=['tm4', 'tm3', 'tm_chop'],
9                                                       direct_mode=True,
10                                                      d_alpha=angsep_rad * np.cos(phi_lin),
11                                                      d_beta=angsep_rad * np.sin(phi_lin))
12
13          return transm_curve_chop, transm_curve_tm4
```

### 5.0.2 Additional graphs

**Habitability**   Figure 26 shows the relative change $R(\delta)$ for different stellar types of the host star, the time optimization scenario 1 and the optimistic and pessimistic instrument scenarios. This complements the results presented in Figure 3.
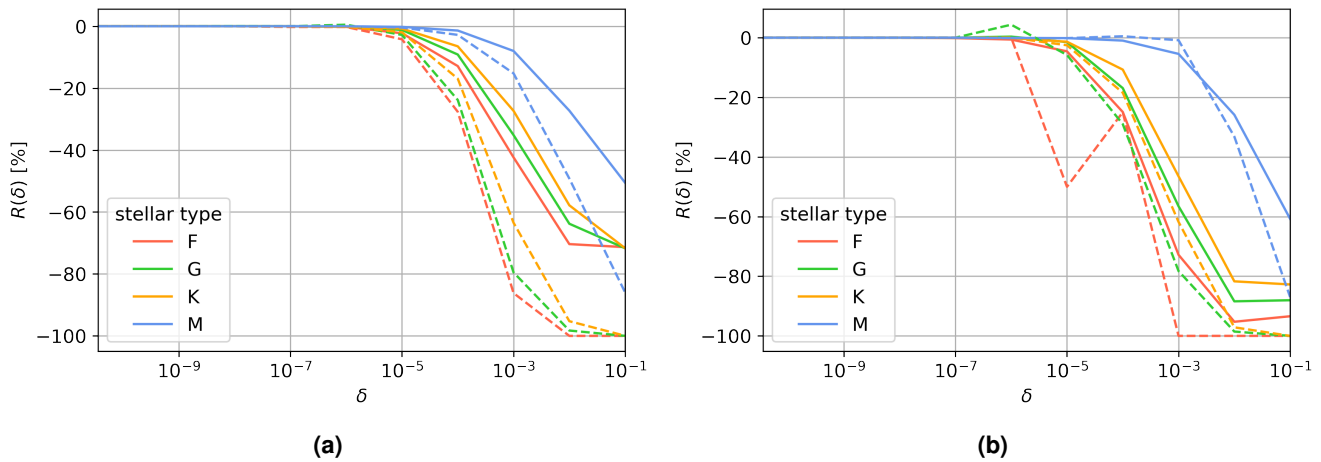


**(a)**  **(b)**

**Figure 26.** Relative change $R(\delta)$ for planets in the HZ (dashed line) or overall (plain line), with the first time optimization scenario and for: (a) the optimistic; (b) the pessimistic instrument configuration.

On the other hand, Figure 27 shows the same results obtained for the time optimization scenario 2, hence complementing Figure 12.



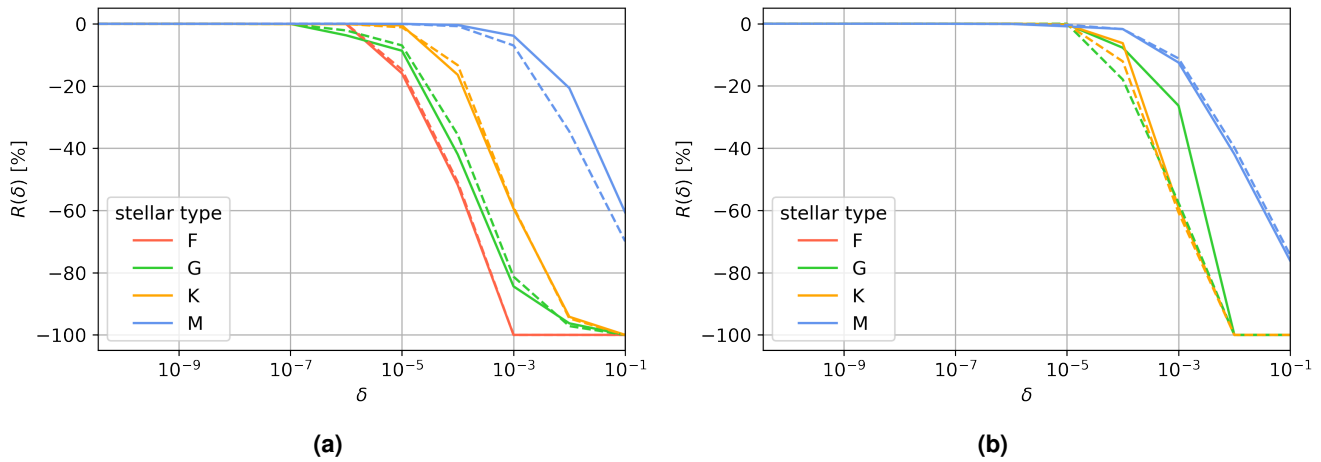**(a)**  **(b)**

**Figure 27.** Relative change $R(\delta)$ for planets in the HZ (dashed line) or overall (plain line), with the second time optimization scenario and for: (a) the optimistic; (b) the pessimistic instrument configuration.

### 5.0.3 Project documents

Please find attached to this work the research plan provided at the beginning of the project as well as the declaration of originality.

RESEARCH PLAN

LIFEsim SEMESTER PROJECT

INSTITUTE FOR PARTICLE PHYSICS AND ASTROPHYSICS

EXOPLANETS AND HABITABILITY GROUP

---

**Measure and characterization of the impact of non-perfect nulls on the detectable planet population by the LIFE space mission, based on different stellar and planetary properties and using the LIFEsim simulator.**

---

*Author*

XAVIER KERVYN
xkervyn@student.etzh.ch

*Supervisors*

DR. SASCHA P. QUANZ
quanzs@phys.etzh.ch

FELIX DANNERT
fdannert@phys.etzh.ch

ETH Zürich, HS 2021

# 1    Motivation

The Large Interferometer For Exoplanets (LIFE) space mission aims at detecting and characterizing the atmospheres of hundreds of nearby extrasolar planets by means of a mid-infrared nulling interferometer concept[1]. The latter would consist of four formation flying collector telescopes with a beam combiner spacecraft at their center.

To quantify the scientific potential and define the technical requirements inherent to LIFE, the team has developed a software tool to simulate LIFE observations: LIFEsim. This allows for a simulation of the instrument and the astrophysical sources. The photon fluxes and signal-to-noise ratio (SNR) of the selected planetary population are eventually computed. To compensate for the imprecision of the instruments, a SNR greater or equal than 7 is required for a planet to be considered detected, instead of the common lower bound value of 5. However, the imperfection of the nulling interferometer induces an incomplete nulling of the different photon noises in the interference fringe pattern, which would inevitably affect the SNR computation and hence the yield detection of LIFE. This study aims at estimating this effect and is thereby a first step taken towards integrating instrumental effects in LIFEsim.

# 2    Methodology

In order to measure the impact of the non-perfect nulls on the signal-to-noise ratio, the model implemented in the software for the transmission maps of the instrument will first be studied. This model has been described by Ottiger et al. [1] and does not take into account the imperfect nulling of the instrument. The transmission function will thus have to be adjusted to accommodate for the aforementioned imperfect nulling. A focus will be given on the intensities of the third and fourth destructive output transmissions modes, respectively $T_3$ and $T_4$, given by

$$T_m = |W_m|^2 = \left| \sum_k U_{m,k} V_k \right|^2,$$

with $m = 3, 4$ the chosen output mode, $V_k$ the input beams to be combined by the interferometer and $U_{m,k}$ the matrix element ($m^{\text{th}}$ row, $k^{\text{th}}$ column) implementing the combination of the beams by the central combiner spacecraft. Different models for $T_{3,4}$ may be taken into account depending on their accuracy on simulating the three different astrophysical noises considered, that are stellar leakage, local zodiacal dust and exozodiacal dust. The differential transmission map $T_{\text{dif}}$, will not be manipulated in this study but will be affected through the relation $T_{\text{dif}} = T_3 - T_4$.

The simulation will be run for different values of the parameter accounting for the imperfect nulling of the interferometer, spanning the model of an ideal interferometer (perfect nulls) to more pessimistic scenarios. This parameter shall be referred to as $\delta$ in the following.

Each time, the instrument settings will be the same as in Quanz et al. [2], that is to say an aperture diameter of 2 m for the telescopes, a ratio between the long and the short baseline of the X-array of 6:1, a $\pi/2$ phase shift applied between two conjugate transmission maps and an observation wavelength spanning 4 $\mu$m to 18.5 $\mu$m ("baseline" scenario). Only FGK and M-stars will be considered. The wavelength setting the angular separation of the instrument will be of 15 $\mu$m and the simulation will be run for two observing time optimization scenarios: full parameter space of detectable planets (scenario 1) or only rocky planets within the empirical Habitable Zone (scenario 2). Hence, the only modified parameter will be the transmission map function (via $\delta$), which should ensure a coherence with the results presented in the latter article.
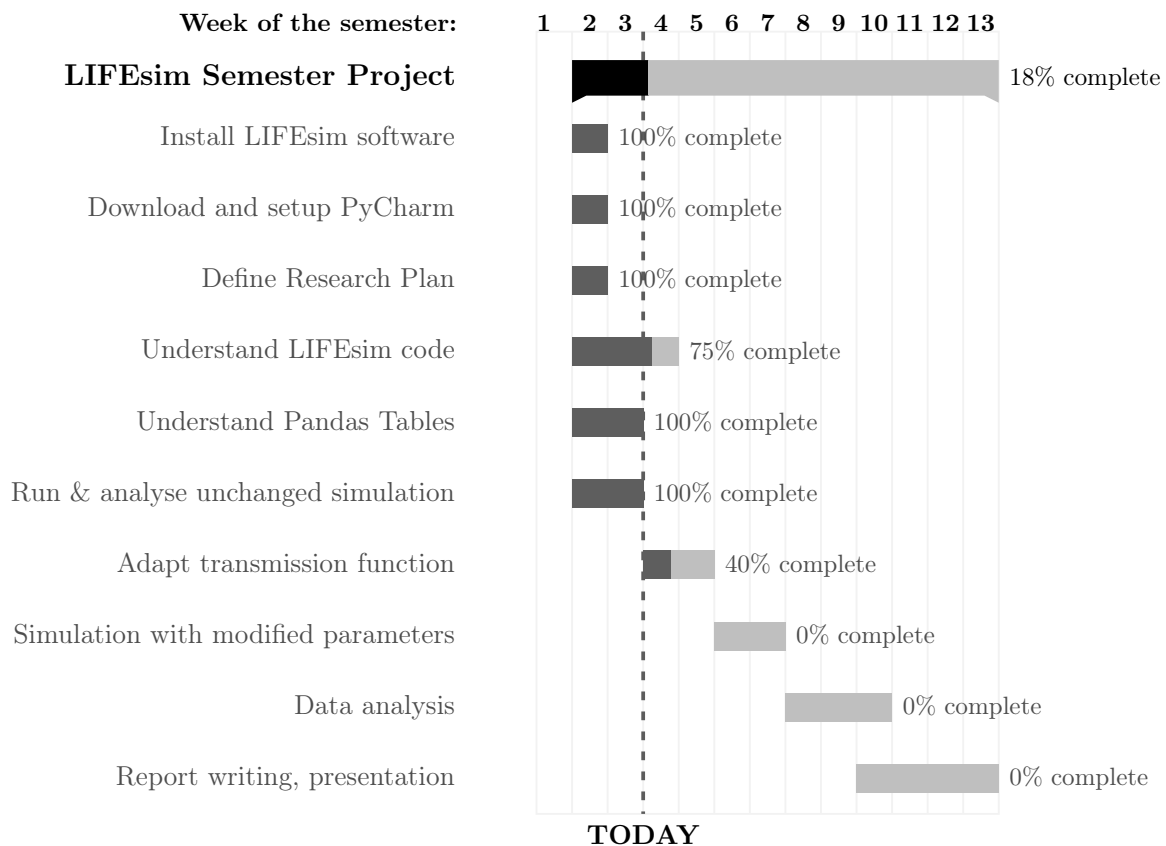
By computing the number of detectable planets for all stars and for different photon noise models, one should be able to quantitatively showcase how the non-perfect nulls affect the

---

[1]https://www.life-space-mission.com/the-project/science/

detection yield of LIFE. A focus will first be given to the distribution of detectable exoplanets as a function of the spectral type of their host star to identify if the photon noise affects the detection of the planets equally or rather depends on the type of their host star. In a second phase, the number of detectable planets will be studied successively as a function of their distance to the instrument, their temperature and their stellar insolation. This should allow a further fine-tuning of the impact of non-perfect nulls on the detectable planet population and provide a quantitative comparison between the detection yields obtained in a range of $\delta$.

## 3    Research Plan and Rough Timeline

This section provides a rough estimation of the duration of the project as well as its organization. The progress bars indicate the actual stage of the project (today = October 11, 2021). The order of the tasks on the left corresponds to the rough timeline of the project.

| Week of the semester: | 1 2 3 4 5 6 7 8 9 10 11 12 13 | |
|---|---|---|
| **LIFEsim Semester Project** | | 18% complete |
| Install LIFEsim software | | 100% complete |
| Download and setup PyCharm | | 100% complete |
| Define Research Plan | | 100% complete |
| Understand LIFEsim code | | 75% complete |
| Understand Pandas Tables | | 100% complete |
| Run & analyse unchanged simulation | | 100% complete |
| Adapt transmission function | | 40% complete |
| Simulation with modified parameters | | 0% complete |
| Data analysis | | 0% complete |
| Report writing, presentation | | 0% complete |

**TODAY**

## 4    Conclusions

This study should provide a quantitative and qualitative comparison of the predicted detection yield of life for different photon noise scenarios. It would then enable to define precise requirements for the instruments to mitigate the consequences of non-perfect nulling and provide the highest number of detectable planets.

### References

[1] Ottiger et al., 2021, The Astrophysical Journal: 'LIFE - II. Signal simulation, signal extraction and fundamental exoplanet parameters from single epoch observations'.

[2] Quanz et al., 2021, Astronomy and Astrophysics: 'LIFE - I. Improved exoplanet detection yield estimates for a large mid-infrared space-interferometer mission'.

## ETH

Eidgenössische Technische Hochschule Zürich
Swiss Federal Institute of Technology Zurich

## Declaration of originality

The signed declaration of originality is a component of every semester paper, Bachelor's thesis, Master's thesis and any other degree paper undertaken during the course of studies, including the respective electronic versions.

Lecturers may also require a declaration of originality for other written papers compiled for their courses.

_____

I hereby confirm that I am the sole author of the written work here enclosed and that I have compiled it in my own words. Parts excepted are corrections of form and content by the supervisor.

**Title of work** (in block letters):

MEASURE AND CHARACTERIZATION OF THE IMPACT OF NON-PERFECT NULLS ON THE DETECTABLE PLANET POPULATION BY THE LIFE SPACE MISSION, BASED ON DIFFERENT STELLAR AND PLANETARY PROPERTIES AND USING THE LIFESIM SIMULATOR.

**Authored by** (in block letters):
*For papers written by groups the names of all authors are required.*

**Name(s):**

KERVYN

**First name(s):**

XAVIER

With my signature I confirm that
  − I have committed none of the forms of plagiarism described in the 'Citation etiquette' information sheet.
  − I have documented all methods, data and processes truthfully.
  − I have not manipulated any data.
  − I have mentioned all persons who were significant facilitators of the work.

I am aware that the work may be screened electronically for plagiarism.

**Place, date**

Zürich, December 6, 2021

**Signature(s)**

*For papers written by groups the names of all authors are required. Their signatures collectively guarantee the entire content of the written paper.*